

Beam observation system and test station for
the LEBIT project

Florian M. Nebel

May 8, 2003

Dedicated to:

My
mother
my family
all the challenges
those who take them
and those who
help

Contents

1	The LEBIT project - An overview	1
1.1	The National Superconducting Cyclotron Laboratory	1
1.2	Towards low energy beams at the NSCL	2
2	Low energy beam transport in LEBIT	5
2.1	Electrostatic ion beam transport	5
2.2	Vacuum system	9
3	Test ion beam	11
3.1	The test ion source	13
3.2	Mass separation with a Wien filter	16
4	Wien filter development	17
4.1	The ideal Wien filter	17
4.2	Realization of the Wien filter	25
4.2.1	The magnetic field	25
4.2.2	The electric field	29
4.2.3	Ion trajectory simulation and mass resolving power	33
4.2.4	Construction	35
4.3	Results of test measurements	39
4.3.1	Magnetic field	39
4.3.2	Temperature Dependence	40
4.3.3	Mass resolving power	42
5	Beam diagnostics	47
5.1	Position Sensitive MCP Detector	47
5.1.1	General properties	47
5.1.2	MCP detectors for LEBIT	48

<i>CONTENTS</i>	iii
5.1.3 MCP measurements	52
5.2 Faraday Cup	55
6 Summary and Conclusion	58
7 Appendix	60
7.1 Appendix A: Electronic wirerings	60
7.2 Appendix B: Data sheets	62

List of Figures

1.1	Overview of the NSCL facility	2
1.2	The LEBIT beamline	3
1.3	Gas stopping station	4
2.1	The LEBIT beam transport system	6
2.2	The beam transport system in the LEBIT room	7
2.3	Simulation of 90 degree deflector and surrounding components	8
2.4	Simulation of beam transport from gas cell to buncher	8
2.5	Schematics of Beam Observation Box	10
3.1	The ion source mounted to the beam line	12
3.2	Photograph of ion source	13
3.3	Schematics of exposed Colutron ion source	14
3.4	Schematics of LEBIT test ion source and supplies	14
3.5	Measurements of ion source properties	15
4.1	Electromagnetic forces in a Wien filter	18
4.2	Calculated beam displacement at the end of an ideal Wien filter	20
4.3	Calculated beam displacement 20cm behind an ideal Wien filter	22
4.4	Calculated beam displacement for a mass 100 beam with finite emittance	23
4.5	Calculated beam displacement for a mass 200 beam with finite emittance	24
4.6	Calculated beam displacement as a function of magnetic field strength	24
4.7	Schematics of simplified Wien filter layout	25
4.8	Schematics for magnetic field simulation in y-z plain	26
4.9	Simulation results for magnetic field in y-z plain	27

4.10	Schematics for magnetic field simulation in x-z plain	27
4.11	Simulation results for magnetic field in x-z plain	28
4.12	Calculated beam displacement as a function of filter length	28
4.13	Wien filter electrode structure as used for simulations	29
4.14	Simulation of unmodified electric field in x-z plane	30
4.15	Simulation of modified electric field in x-z plain	30
4.16	Simulation of electric field in y direction	31
4.17	Simulation of electric field in z direction for 9mm gap	32
4.18	Simulation of electric field in z direction for 5mm gap	32
4.19	Wien filter mass resolving power	34
4.20	Simulation result for Argon	34
4.21	Wire frame of the Wien filter	36
4.22	Photograph of Wien filter back side	37
4.23	Photograph of exposed Wien filter front	38
4.24	Measurement of magnetic field	39
4.25	Measurement of temperature dependance	41
4.26	Temperature dependent saturation magnetization of Nickel	42
4.27	Measurement of mass resolving power for 5keV	43
4.28	Measurement of mass resolving power for 1.5keV	45
5.1	Schematics of chevron stack of MCPs	48
5.2	Schematics of MCP detector system	49
5.3	Photograph of MCP mounted on 6" flange	50
5.4	Photograph of mounted CCD camera	51
5.5	Image of average beam spot	52
5.6	Image of focused beam spot	53
5.7	3D plots of beam images	54
5.8	Image of the anchor	54
5.9	Schematics of double sided Faraday cup	55
5.10	Photograph of Faraday cup during assembly	56
5.11	Photograph of assembled Faraday cup	57
7.1	Schematics of safety wiring for MCP detector	60
7.2	Schematics of MCP electric connection	61

List of Tables

4.1	Comparison between calculated and simulated displacement	33
4.2	Wien filter properties	35
5.1	Lens setting for focus in BOB3	53
7.1	Camera properties summary	62
7.2	MCP properties summary	63

Chapter 1

The LEBIT project - An overview

1.1 The National Superconducting Cyclotron Laboratory

The National Superconducting Cyclotron Laboratory is the leading research facility for rare radioactive isotopes in the US [1]. It is a fragmentation facility, located at Michigan State University. Fragmentation facilities produce radioactive isotopes at high energies by accelerating a stable ion beam onto a thin target.

Fig. 1.1 gives an overview of the NSCL facility. Ions are initially produced by an Electron Cyclotron Resonance (ECR) ion source [2]. This source produces a stable beam of 20+ charged ions at low energies (26keV). Electrostatic fields guide the ions to the smaller of the two cyclotrons, the K500. It was the first superconducting cyclotron ever built and accelerates the beam to 12.5MeV/nucleon and sends it towards the second cyclotron. In the injection channel, the beam passes a carbon foil, where almost all remaining electrons are stripped of. The highly charged beam enters the second cyclotron (K1200), which is accelerating the beam to its final energy of about 140MeV/nucleon (corresponding to 18.7GeV for $^{134}\text{Xe}^{+48}$).

Once the beam is ejected from the K1200 it hits a fixed target. Fragmentation and fission reactions occur in the target, producing unstable isotopes. For most experiments only a single rare isotope is of interest. Therefore the reaction products are separated from each other. This is achieved by the

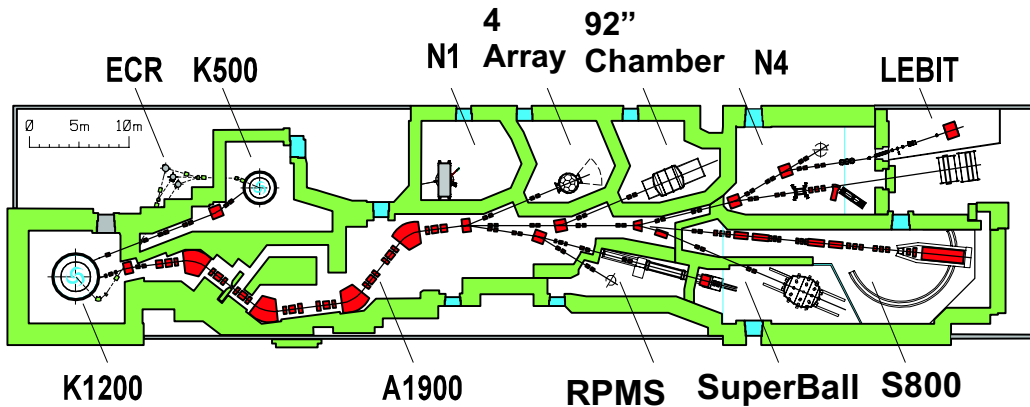


Figure 1.1: Overview of the NSCL facility. A primary stable beam from one of the ECR ion sources is sent to the K500 where it is pre-accelerated. Final acceleration to energies up to 140MeV/u takes place in the K1200, before hitting a thin target. The reaction fragments are separated by the A1900 and delivered to the experiments.

A1900 fragment separator [3], a mass separator capable of selecting one desired nuclei out of 10^{18} different fragments. The clean beam of exotic nuclei is delivered to one of the eleven experimental stations currently supported by the laboratory.

Research at the NSCL is focusing on nuclear structure and nuclear astrophysics. The main experimental approach are nuclear reaction studies. The two story high S800 magnetic spectrograph for example is dedicated to nuclear reaction and decay studies. It is using a magnetic field to determine energy, position and angle of reaction products from the A1900. Unlike other experiments it is able to accept a large number of different reaction products. In addition to the information obtained from reaction studies, the S800 also observes decays of unstable exotic nuclei, to improve understanding of nuclear structure and quantum mechanics.

1.2 Towards low energy beams at the NSCL

A different approach to produce rare isotopes is the Isotope Separator On-Line technique. These accelerators produce low energy beams, as they are required for some precision experiments, like Penning trap mass measure-

ments, decay studies or laser spectroscopy. ISOL facilities rely on chemical diffusion methods to extract the reaction products from the target. This limits the method to create only a certain number of isotopes. A fragmentation facility, like the NSCL, on the other hand uses only physical methods to extract the reaction products from the target, and can access a much larger range of isotopes. In order to have low energy precision experiments at a fragmentation facility it is necessary to slow down the beam. At the NSCL this is done at the **Low Energy Beam and Ion Trap** [4]. Fig. 1.2 gives an overview of the project.

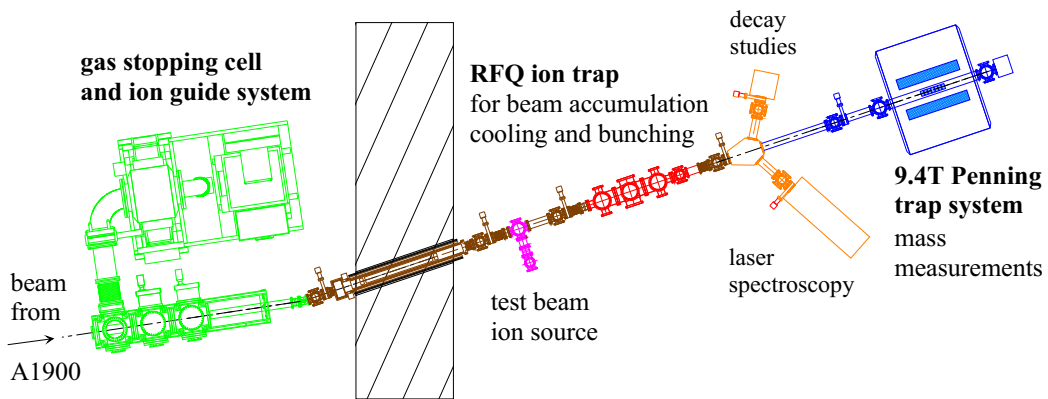


Figure 1.2: Layout of the LEBIT beamline. The high energy beam from the A1900 fragment separator arrives in the N4 vault and is slowed down to low energies by the gas stopping station. Beam is transported electrostatically through the shielding wall into the LEBIT room, where it is delivered to a Penning trap for high precision mass measurements.

The first part of LEBIT is the gas stopping cell. Fig. 1.3 gives an overview of how the beam is slowed down within a gas cell. The high energy of the incoming beam is initially reduced by a solid degrader. The slowed beam enters a gas cell and is stopped by collisions with Helium. Helium has the highest ionization potential of all elements, which reduces the chance of charge exchange.

Other projects currently underway that use gas stopping cells to slow down radioactive beams are: SHIPTRAP at GSI, Germany [5], the Canadian Penning Trap at Argonne National Laboratory, USA [6] JYFLTRAP at the University of Jyväskylä, Finland [7] and MAFFTRAP at FRM-II, Ger-

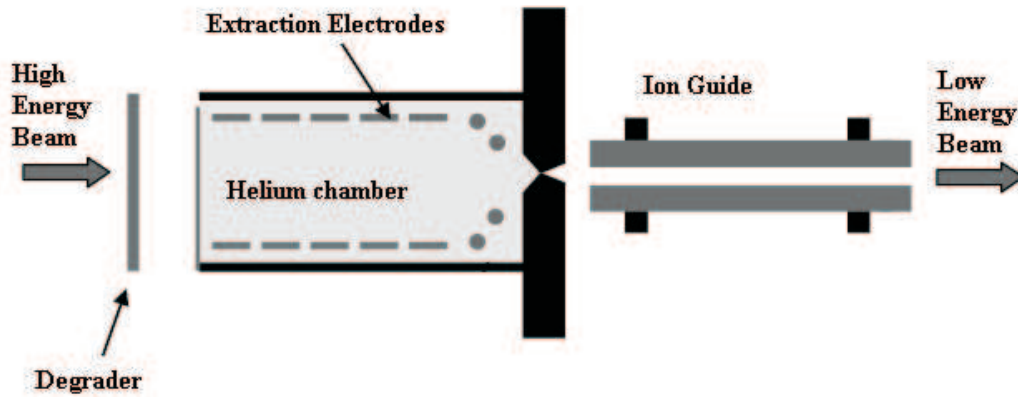


Figure 1.3: Concept of any device dedicated to stop high energy beams. The degrader slows down the beam, that is finally brought to rest inside a Helium filled volume. Electric radio frequency fields guide the stopped ions out of the Helium chamber and re-accelerate them to the desired low energy.

many [8]. The different projects vary in the energy of the incoming beam, and therefore use different gas cell sizes, Helium pressures, and extraction methods.

Once stopped the ions are extracted and guided to **Ultra High Vacuum** ($<10^{-8}$ mbar) by radiofrequency ion guides, where an electrostatic beam transport system guides the beam to the cooler and buncher. The beam observation system helps to maintain good beam quality along the way.

The cooling and bunching device is a combination of linear ion guide and ion trap, based on the radio frequency quadrupole concept [9]. Once again, Helium is used to slow down, cool and bunch the ions to bunches with a small energy spread. A novel feature will be the possibility to cool the buffer gas down to the temperature of liquid nitrogen to reduce the thermal energy distribution.

The bunched low energy beam is finally transmitted to the experimental stations. The first experiment benefitting from the low energy beam will be a 9.4T Penning trap [10], for high precision mass measurement. The mass determination in Penning traps is based on the measurement of the cyclotron frequency of an ion stored in a strong magnetic field. LEBIT will use a 9.4T magnet instead of the commonly used 6T to 7T magnets, which will increase the measurement precision by a factor of two.

Chapter 2

Low energy beam transport in LEBIT

A beam transport section is used to guide the beam from the gas cell through the shielding wall to the cooler and buncher. The beam energy of 5keV makes both magnetic and electrostatic beam transport feasible. A magnetic system is used by the NSCL to guide its high energy beams, while for the LEBIT low energy beam line an electrostatic system is used. It is not mass dependent and there is no need to adjust lens settings if a beam with a different mass is used. Also electrostatic lenses are easier to build and operate compared to the magnetic system.

To reduce the loss in ion beam intensity, due to particle scattering, LEBIT is operating under ultra high vacuum. Vacuum quality needs to be monitored at all times. For this purpose the beam transport section will have vacuum gauges installed along the beam line.

2.1 Electrostatic ion beam transport

Fig. 2.1 shows the beam transport section, that is used to transport the beam from the N4 vault, where the gas cell is located, to the LEBIT room. The section includes a 90 degree deflector with a test ion source attached.

To guide the beam electrostatic Einzel lenses are used. The idea is to focus the beam on certain spots and observe the focus. The position of the focus is controlled with the beam observation system. Lens settings can be adjusted to improve the focus if needed. The beam observation detector

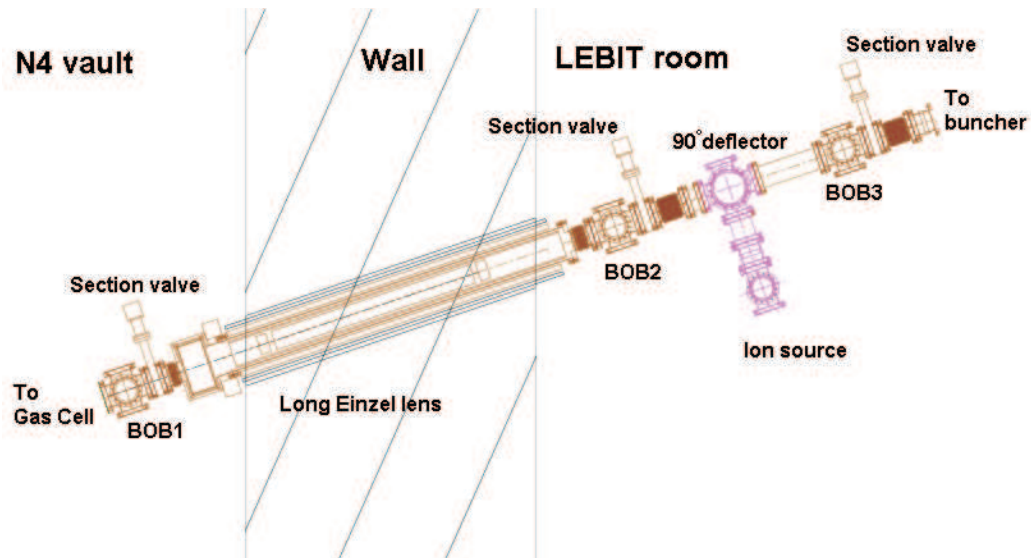


Figure 2.1: Beam transport section. Stopped ions are re-accelerated to 5keV and guided by electrostatic means to the buncher section. BOBs allow beam observation along the way

system, allows measurement of beam position and intensity. It is installed inside the so called **B**eam **O**bservation **B**oxes (BOB).

The first focal point is inside the first Beam Observation Box (BOB1) at the beginning of the beam transport system. It is followed by the "Long Einzel lens" installed in the shielding wall that separates the N4 vault from the LEBIT room. Once the beam arrives at the LEBIT room, its properties are measured inside BOB2. A picture of the beam transport section in the LEBIT room is shown in fig. 2.2.

After BOB2 another lens focuses the beam inside the 90 degree deflector, which is followed by a third Einzel lens focusing the beam into the buncher. There is no focus in BOB3 but the beam image allows for control of the ion injection.

The 90 degree deflector makes it possible to send a stable beam produced by the ion source upstream and downstream.

Fig. 2.3 and 2.4 both show results of beam transport calculations with SIMION [11]. SIMION uses an iterative method to solve the Laplace equation for given boundary conditions. Fig 2.3 shows a three dimensional overview

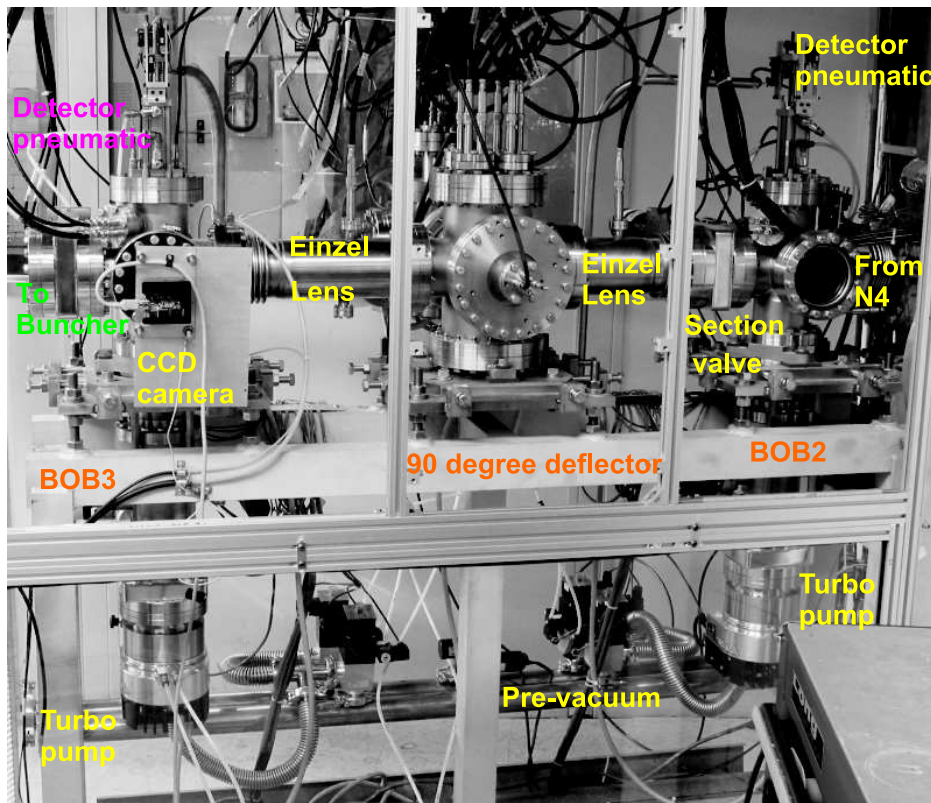


Figure 2.2: BOB2 is installed next to the wall and receives the beam from the long Einzel lens. After focusing the beam into BOB2, two Einzel lenses guide the beam through the 90 degree deflector to BOB3 and further on to the buncher. The ion source is attached on the back side of the 90 degree deflector.

of the 90 degree deflector and its surrounding components. The picture includes beam from the ion source and heading towards the buncher. Fig. 2.4 contains the preliminary result of the beam transport simulation from BOB1 to BOB3.

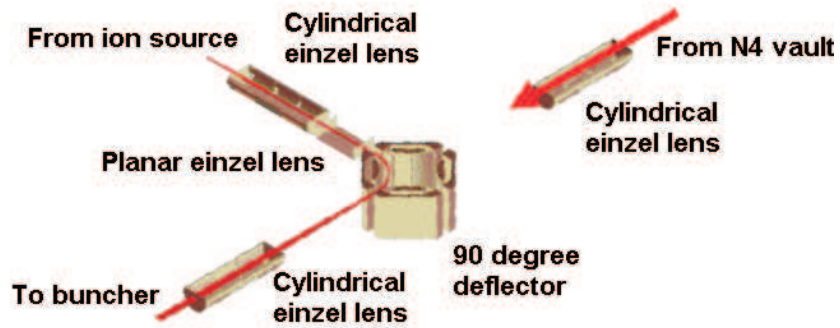


Figure 2.3: Simulation of 90 degree deflector and surrounding components. Beam can be bend up or downstreams. Cylindrical Einzel lenses focus the beam.

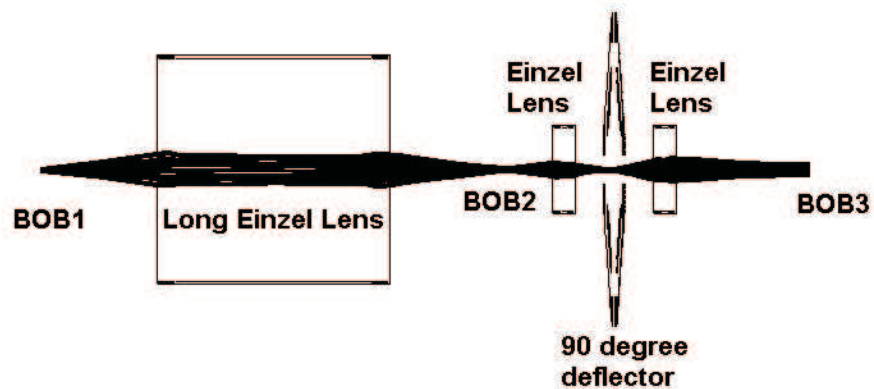


Figure 2.4: Beam transport simulation. The beam from the gas cell is focused into BOB 1 and 2 with an intermediate focus inside the 90 degree deflector.

2.2 Vacuum system

The overall concept chosen for the beam line was to have different vacuum sections, each of them terminated by a BOB and a gate valve. This design protects the rest of the vacuum line, if only one section has a malfunction. For maintenance work or upgrading, only one section needs to be filled with air. As a future option, control software can be used to combine valve controls with vacuum gauge readouts to guarantee that no operation can be committed that would jeopardize the vacuum.

Each BOB functions primarily as a pumping station and is equipped with a turbo pump (Leybold TW300) as seen in Fig. 2.5. Each turbo pump connects to two pre-vacuum lines via electropneumatic valves. Having two pre-vacuum lines allow each BOB to be pump individually without disconnecting the others. This is especially useful, when a single vacuum section is being pumped down and the others are already under vacuum.

For pressure measurement, a BOB has a cold cathode Penning gauge and a Pirani gauge installed, to cover the entire pressure range. Each of the pre-vacuum lines has a Pirani gauge connected. All gauges are manufactured by MKS vacuum systems. Without baking the vacuum chambers, pressures of 10^{-8} mbar to 10^{-9} mbar could be reached.

Vacuum and beam transport parts of a BOB are separated by a ceramic insulator, making it possible to operate gauges and pump on ground potential while the rest of the beam line is on high voltage. Electric insulation of the vacuum line from the support structure is achieved by additional insulators.

Furthermore, each BOB is equipped with two pneumatic devices to insert and remove beam observation detectors. This pneumatic requires compressed air and a remote signal before it starts moving the detector in. To avoid one of the detectors remaining inserted when air or signal are lost, a strong spring is installed to move the detector out. A hardware safety wiring prevents both detectors from moving in at the same time.

A detailed discussion of the installed detector systems will be given in chapter 5.

Finally the steering electrodes allow the beam position to be changed if required.

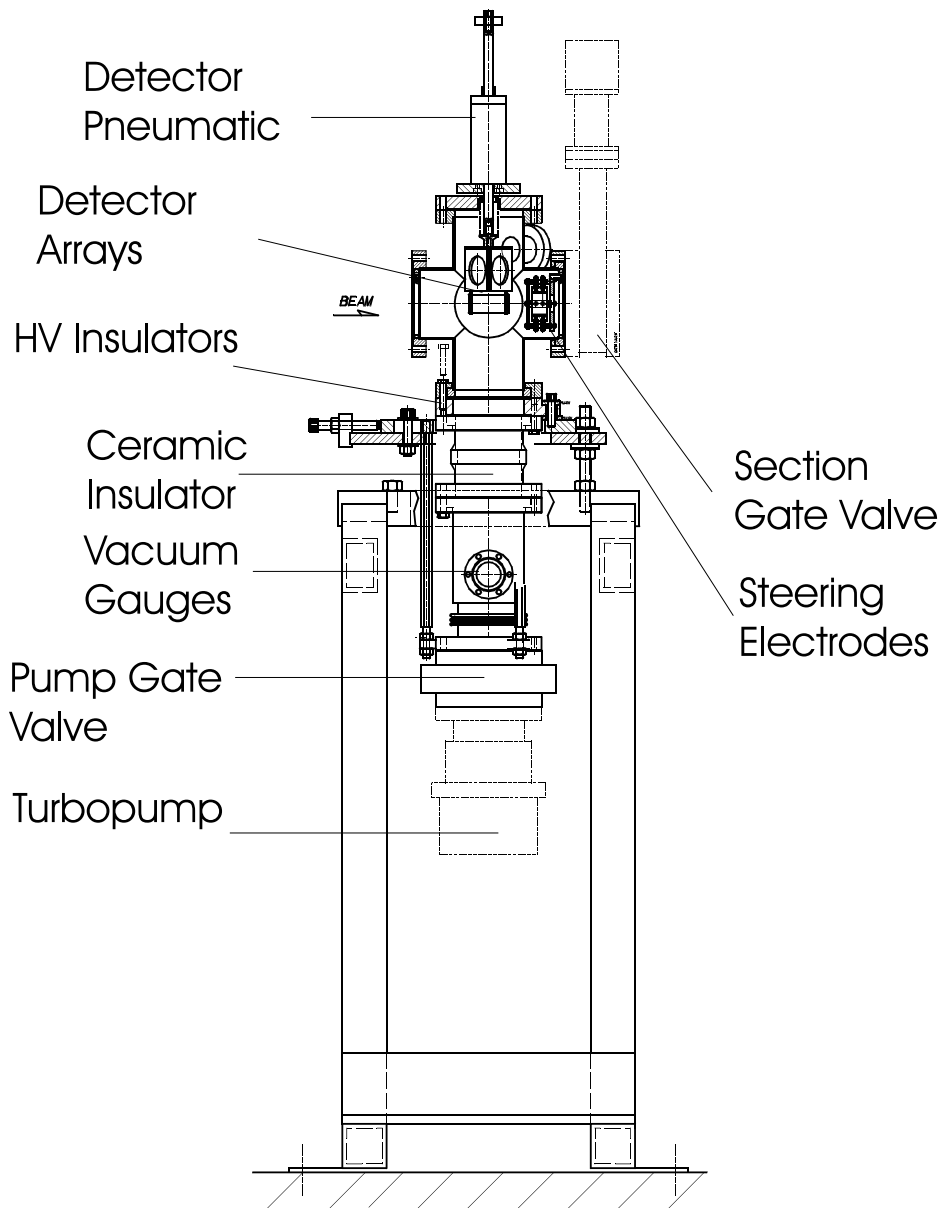


Figure 2.5: Schematics of beam observation box. Detector pneumatics are used to move beam observation detectors in and out. The insulators separate high voltage from ground potential. The section gate valve allows separation of the beam line in sections.

Chapter 3

Test ion beam

Beam from the A1900 will only be available during beam times. In order to test LEBIT components independent from the A1900, LEBIT has its own ion source for stable ion beams. It is attached perpendicular to the main beam line as shown in fig. 2.1. Stable test ion beams are needed for two reasons:

- a) Testing and optimization of ion optics including ion trap
- b) Calibration of magnetic field of the Penning trap

For the first purpose, the beam produced can be sent upstream and downstream by means of the 90 degree deflector. This pilot beam can be used to check the alignment of ion optical components. Using the beam observation system in the BOBs it is possible to determine if the beam is well aligned and to correct lens voltage settings if necessary. Also the beam observation system, the Penning trap, the cooler and buncher can be tested in this way.

The second purpose is the calibration of the magnetic field of the LEBIT Penning trap. In order to be able to make high precision mass measurement with the Penning trap, the magnetic field inside the trap must be known. For this purpose the cyclotron frequency of a stable isotope is measured. The demands on an ion source for this purpose are a reliable, easy to operate source capable of producing different beams. This requirement can be met using a plasma ion source. The mechanism used is electron impact ionization, and, as a result, such sources are not very element selective. That means that they can deliver a large variety of test beams.

For the optimization of the parameters of the cooler and buncher, but also for the calibration of the Penning trap it is of advantage to have a mass separated beam, since the operating parameters of these devices are mass dependent. Various approaches could be utilized to achieve mass separation with a modest resolving power. Part of this thesis work was the construction and test of a Wien filter for this purpose.

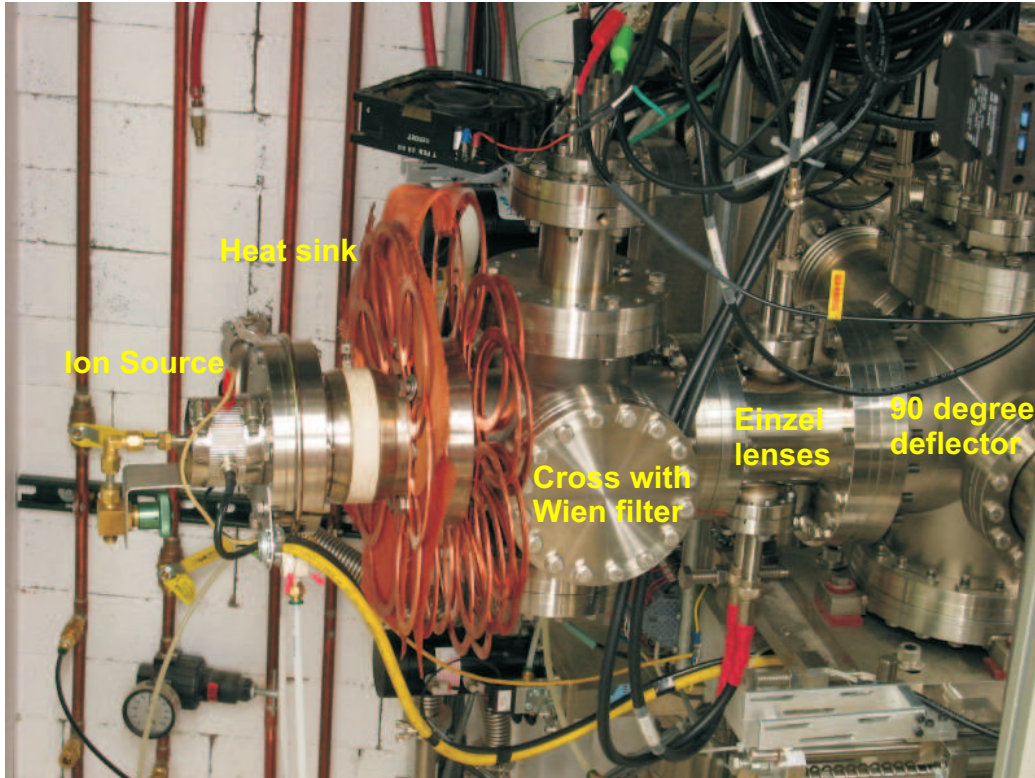


Figure 3.1: Beam line extension at the 90 degree deflector. The heat sink is necessary to provide cooling for the ion source and Wien filter.

Fig. 3.1 shows a picture of the beam line extension including (from left to right) the ion source, the Wien filter installed in the first cross, and the 90 degree deflector. Parts of the main beam line can also be seen. The large heat sink, made of used conflat gaskets, is a preliminary solution to keep the ion source as cool as possible and to provide stable operation conditions for the Wien filter.

3.1 The test ion source

The source used is a Colutron Model 101-O [12]. It is a discharge source and equipped with an oven that can be heated up to 2000K to vaporize solid materials. According to the manufacturer the produced beam has an energy spread of 0.11eV and can be as intense as $2\mu\text{A}$. Having a beam current in the microampere range is unnecessary high for any applications considered for LEBIT, but it still has an advantage. The beam quality can be improved further by reducing the beam diameter, what also decreases the beam intensity.

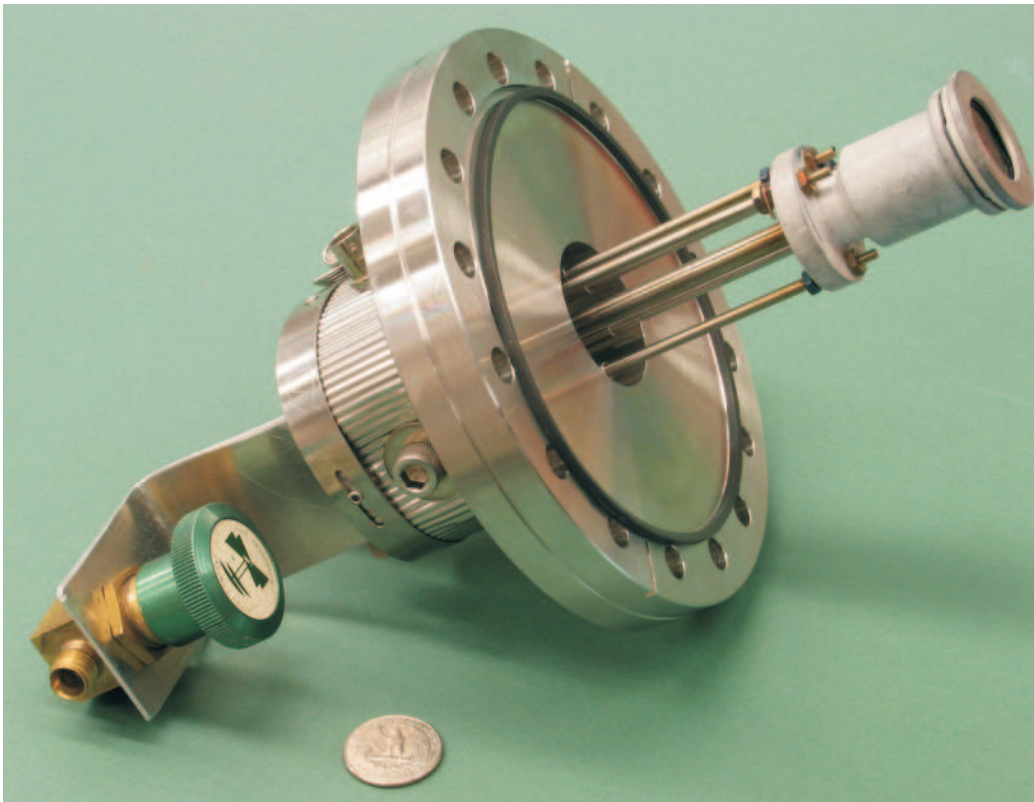


Figure 3.2: Picture of the ion source mounted on a 6''-conflat flange. A needle valve connected to the gas inlet is visible on the left.

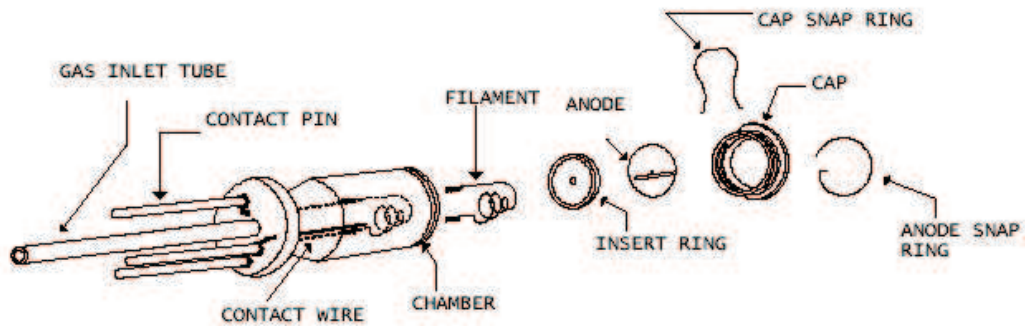


Figure 3.3: Exposed view of the ion source. Gas is let in via inlet tube. Electrons from the hot filament cathode ionize gas inside the boron nitride chamber, while they are accelerated towards the anode.

Fig. 3.2 shows a picture of the ion source mounted on a 6" conflat flange. The schematics in fig. 3.3 represent an exposed view of the ion source. The cap, the insert ring and the chamber are made from boron-nitride (BN), the other parts are made from stainless steel. The filament is constructed from tungsten wire and functions as a hot cathode for electron production. The electrons are accelerated towards the anode. Depending on the acceleration voltage and the gas used, a single electron can ionize one or more particles.

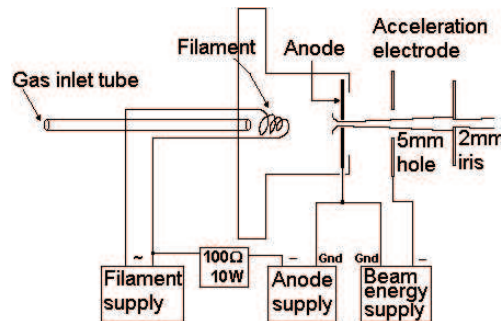


Figure 3.4: LEBIT test ion source and supplies. The tungsten filament is connected to an AC power supply. The anode supply adds an additional DC potential between anode and filament to accelerate electrons. The Beam power supply provides the acceleration voltage. The ion beam is limited to a diameter of 2mm by an iris.

Fig. 3.4 shows the schematics of the source including its suppliers. The acceleration electrode is placed 24mm after the anode and has a 5mm hole. It is followed by a 2mm diameter iris to limit beam size, before it enters the Wien filter.

The ion current produced by the source depends mainly on four parameters. Gas pressure and type, anode voltage and filament current. The latter two have major influence on the anode current. The manufacturer suggests operating the source with 30V to 100V anode voltage and up to 150mA anode current adjusted only by the filament current.

After installation of the ion source, primary test measurements were performed to characterize its performance and properties. The Wien filter was already installed and set to mass 28 for Nitrogen. The beam was collected with a Faraday cup.

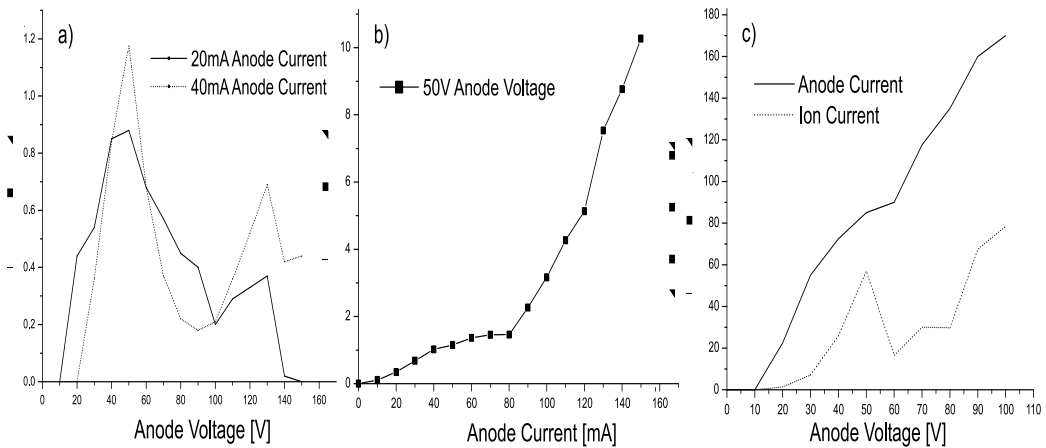


Figure 3.5: Ion source current as a function of a) anode voltage for different Anode Currents and b) anode current for constant anode voltage. Graph c) shows anode current and ion current as a function of anode voltage for fixed filament current.

Fig. 3.5 shows results of measurements for Nitrogen under constant pressure. Graph 3.5 a) illustrates the effect of the anode voltage on the ion current. The anode current is kept constant by varying the filament current. Maxima appear for 50V and 130V. The reason is energy dependent ionization cross sections.

Fig. 3.5 b) shows how the ion current changes with the anode current for constant anode voltage. Filament current is varied to change the anode current. Ion current rises, as expected for higher filament current.

Fig. 4.1 c) illustrates how anode current and ion current depend on the anode voltage for fixed filament current. While the anode current has two maxima again, the ion current does not show any. The reason is the same as in fig. a)

These results do not represent the general behavior of the source but give an idea as to how it works. The behavior of the source changed every time modifications were made to it. Specifically, replacing of burned filaments lead to a drastic change in beam quality. More research is required to completely understand the behavior of the source.

3.2 Mass separation with a Wien filter

To achieve mass separation of the test ion source beams, it was decided to use a Wien filter. First introduced by W. Wien [13] in 1898, this velocity filter allows in-flight mass separation for ion beams with constant kinetic energy. It is feasible in the energy range desired for LEBIT and uses a combination of magnetic and electric fields. The electric field is a static field and therefore easy to generate. For the magnetic field, permanent magnets or electro magnets can be used. The latter require large coils and cooling, especially inside a vacuum, where heat can only be radiated. Permanent magnets, on the other hand, produce no heat, require no wiring and use less space. Since the LEBIT Wien filter should be a compact device, permanent magnets are used. New developments in permanent magnet production offer reasonable strong fields. Neodymium-iron-boron magnets are the strongest magnets available, having a residual induction varying from 1.0T to 1.4T.

Using a permanent magnetic field the electric field and the beam energy are the only variables to be adjusted. The next chapter will deal in detail with the development of the LEBIT Wien filter. A smaller Wien filter using permanent magnets was developed by Numela [14].

Chapter 4

Wien filter development

4.1 The ideal Wien filter

The velocity dependence of the Lorentz force is used for mass separation in a Wien filter. To allow in-flight mass selection, a Lorentz force F_L and an electric force F_E are superposed as shown in fig. 4.1. The Lorentz force is directed perpendicular to the magnetic field and the ion's velocity while the electric force is parallel to the electric field. An ion with the charge q and velocity v , travelling perpendicular to both fields passes the filter without displacement if both forces have equal magnitude and opposite direction.

$$\vec{F}_E - \vec{F}_L = 0 \quad (4.1)$$

$$qE = qvB \quad (4.2)$$

$$v = \frac{E}{B} \quad (4.3)$$

For a given kinetic energy K the velocity of an ion depending on mass m is

$$v = \sqrt{\frac{2K}{m}} \quad (4.4)$$

Therefore the Wienfilter is mass selective if all the ions that enter have the same kinetic energy and charge. Using equation 4.3 and 4.4 only ions with mass

$$m_0 = 2 \frac{B^2}{E^2} K \quad (4.5)$$

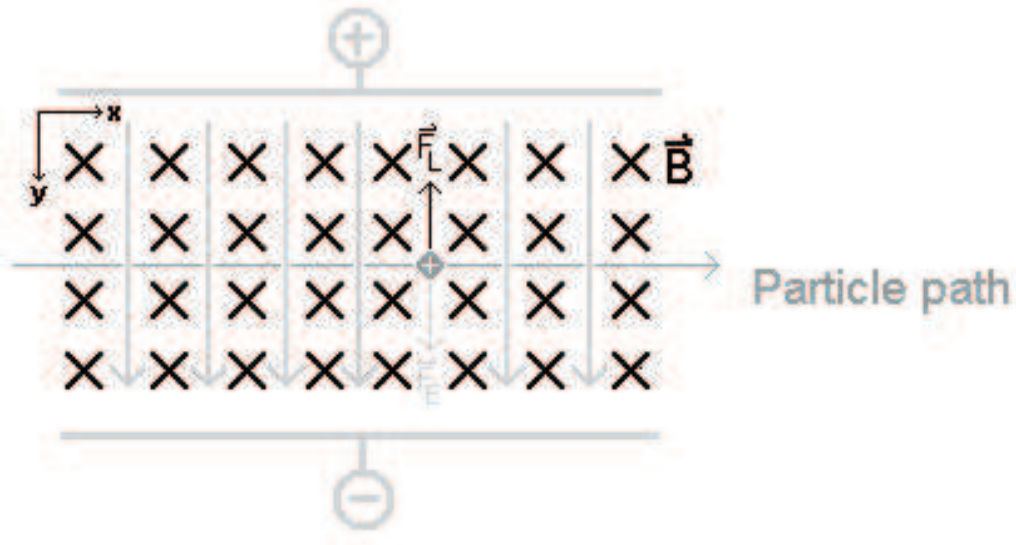


Figure 4.1: Electromagnetic forces in a Wien filter. Magnetic (F_L) and electric force (F_E) are acting in opposing directions. For equal forces the ion passes undeflected.

are able to pass undeflected. All other ions are deflected and can be stopped at a slit.

Calculating the path of the deflected ions is more demanding. Equation 4.1 is true for an ion passing straight through the filter. For heavier or lighter ions a net force remains accelerating the ion in a direction perpendicular to its initial velocity, therefore separating it from ions with mass m_0 .

$$m\vec{a} = \vec{F}_E - \vec{F}_L \quad (4.6)$$

With $\mathbf{B}=(0,0,B_z)$, $\mathbf{E}=(0,E_y,0)$ and $\mathbf{v}=(v_x,v_y,v_z)$ equation 4.1 can be written as a set of three equations

$$m\ddot{x} = qv_yB_z \quad (4.7)$$

$$m\ddot{y} = qE_y - qv_xB_z \quad (4.8)$$

$$m\ddot{z} = 0 \quad (4.9)$$

The ions propagate in the x direction and are deflected in the y direction. This set of differential equations can be solved using standard techniques [15] [16]. The solutions are

$$x = \frac{E_y}{B_z}t + y'_0 r [1 - \cos \omega_c t] - rG \sin \omega_c t \quad (4.10)$$

$$y = y_0 + y'_0 r \sin \omega_c t + rG [1 - \cos \omega_c t] \quad (4.11)$$

With y_0 being the initial y position and t being the time the ions spend in the filter. The following abbreviations are introduced:

The cyclotron frequency,

$$\omega_c = q \frac{B_z}{m} \quad (4.12)$$

the curvature,

$$r = \frac{mv_{x0}}{qB_z} \quad (4.13)$$

the velocity ratio,

$$G = \frac{E_y}{B_z v_{x0}} - 1 \quad (4.14)$$

and the initial velocity slope defined as

$$y'_0 = \frac{v_{y0}}{v_{x0}} \quad (4.15)$$

Equation 4.11 shows the time dependent displacement of ions with mass m for a straight line motion. Ions with mass m_0 will pass undeflected. In order to calculate the total x dependent displacement of the ions by the Wien filter the explicit time dependence needs to be eliminated. Therefore equation 4.10 needed to be inverted. An analytical solution to this problem is not known, but an approximation can be used, since the sine and cosine terms in 4.10 are only adding minor modifications to the linear part $K=5\text{keV}$ and $B=1.2\text{T}$ lead to $E_y/B_z=1.07 \cdot 10^5$, while y_0 'r and rG are in the order of $5 \cdot 10^{-4}$. Therefore, the non linear terms can be discarded. Consequently t can be written as

$$t \approx \frac{B_z}{E_y} x \quad (4.16)$$

Using equation 4.16, 4.11 becomes:

$$y = y_0 + y'_0 r \sin\left(\omega_c \frac{B_z}{E_y} x\right) + rG \left[1 - \cos\left(\omega_c \frac{B_z}{E_y} x\right)\right] \quad (4.17)$$

Fig. 4.2 shows how an ion with mass $m+1$ will be displaced with respect to mass m that passes undeflected (For $m=50u$, $100u$ and $200u$). The displacement is shown as a function of the position x in the Wien filter. To make things easier y_0 and y_0' are 0, the beam energy is $5keV$. The magnetic field strength is $B=1.2T$.

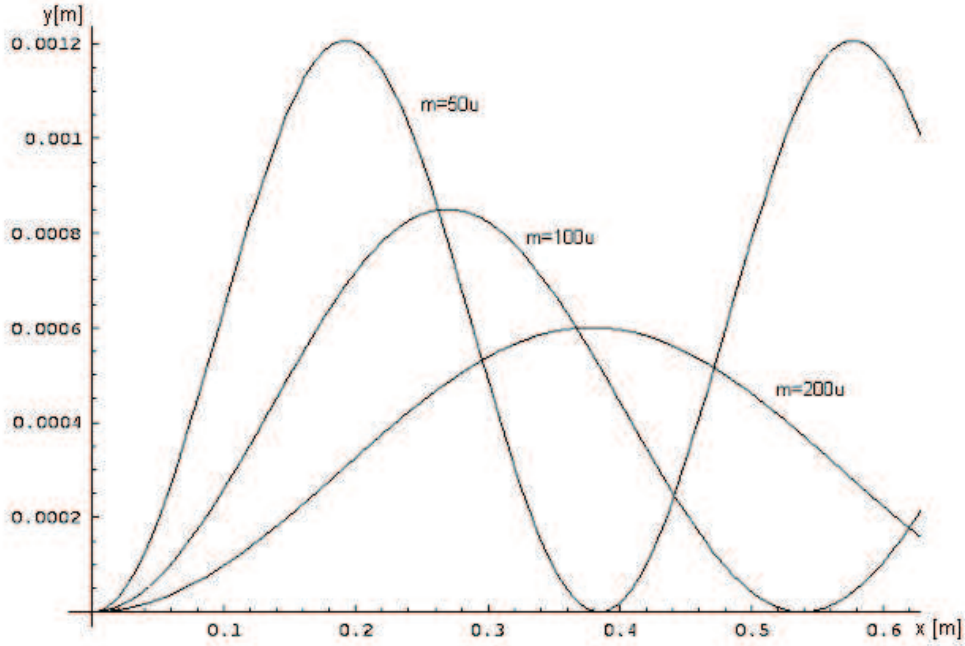


Figure 4.2: Displacement y at the end of the filter with a length x for masses $m=50u$, $m=100u$ and $m=200u$. The magnetic field strength and kinetic energy used are $B=1.2T$, $K=5keV$. Initial velocity and velocity slope are $y_0=y_0'=0$.

Ions inside a Wien filter that do not have the mass m_0 follow a sinusoidal curve. Lighter masses reach maximum displacement earlier and the magnitude of the displacement is larger. Once the maximum is reached, the ions are bent back towards the symmetry axis. Therefore maximum displacement for a specific mass is linked to an optimum magnetic field value for a given filter length. When choosing how long the filter needs to be for a given magnetic field it is necessary to make a compromise between different masses and desired displacements for those masses.

For ion beams with zero emittance and an ideal Wien filter, the y displacement is the only parameter determining how far two masses can be separated. In a filter with displacement possibilities as shown in 4.2 and a length of $x=120\text{mm}$ an ion with $m=201u$ is deflected by 0.6mm from an ion with $m=200u$, while the ions with mass $50u$ and $51u$ would be separated by 1.2mm . A 2mm wide slit stops ions with mass $51u$ but ions with mass 200 and 201 would pass unseparated. Adding a smaller slit can improve mass separation, while transmission is reduced.

To increase the displacement of heavier ions it is possible to place the slit further behind the filter. Taking a distance D between the filter and the slit makes the slope of the trajectory at the end of the filter the parameter which determines the separation. The point of maximum slope is reached before the point of maximum displacement, what can be used to reduce the length of the filter. After the filter ions travel a distance D and the resulting displacement $y_D(x)$ is given by

$$y_D(x) = y(x) + Dy'(x) \quad (4.18)$$

where x is the length of the filter, $y(x)$ is the displacement at the end of the filter and

$$y'(x) = r\omega_c \frac{B_z}{E_x} (y'_0 r \cos(\omega_c \frac{B_z}{E_x} x) + G \sin(\omega_c \frac{B_z}{E_x} x)) \quad (4.19)$$

is the slope of the ion's trajectory at the end of the filter.

For $m=50u$, choosing $D=20\text{cm}$ the displacement increases to 2.17 times the displacement achieved for $m=50u$ with $D=0$ and the necessary filter length for maximum displacement is reduced by a factor of 2 . This is shown in fig 4.3.

Fig. 4.3 also illustrates that a negative displacement is possible for this Wien filter setting, since the slope of the ions path inside the filter is now the important factor. While deflection to negative y values at the end of the filter is impossible, negative slope is and can lead to a displacement in the direction of the negative y axis after the distance D .

The beam coming from the ion source is not as perfect as assumed so far, but has a finite beam diameter Δy and direction spread $\Delta\alpha$. The product $\Delta y\Delta\alpha$ is called emittance and affects the mass resolution of the filter.

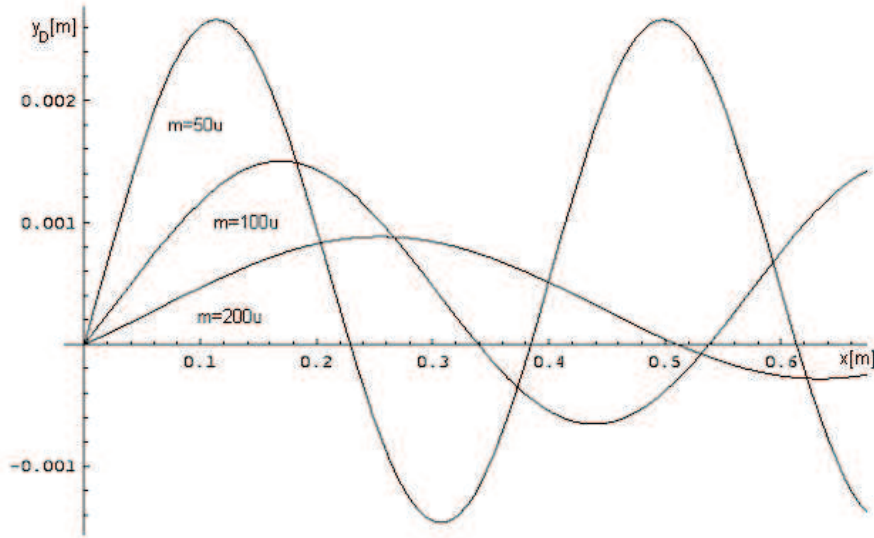


Figure 4.3: Displacement y_D as a function of the Wien filter length x observed at the distance $D=20$ cm behind the filter.

Mass resolution is defined as the minimum mass difference that can be separated for a given mass and charge. Resolving power is the mass divided by the resolution. Assuming a rectangular beam profile, two beams can be separated as long as their paths do not overlap at the detector.

Using an emittance of 2π mm mrad for the ion source as claimed by the manufacturer, the $y_D(x)$ diagrams look like fig 4.4 and 4.5.

As can be seen from fig. 4.4 and 4.5, neighboring masses up to 100u can be separated easily with a 120mm long filter and heavier masses with careful choice of parameters.

A strong magnetic field is required to provide good resolution for larger masses, but it is not necessarily advantageous for the separation of light nuclei. Fig. 4.6 illustrates this problem. It shows the dependence of the displacement y_D from the magnetic field strength for three different mass pairs for a fixed filter length of 12cm and $D=20$ cm

Due to the fact that a permanent magnet is used, the filter cannot have optimum mass resolution for the complete mass range. Therefore, for a fixed magnetic field, in the order of $1.0T \pm 0.2T$, a filter length needs to be chosen that delivers good mass resolution for the desired mass region. A length of

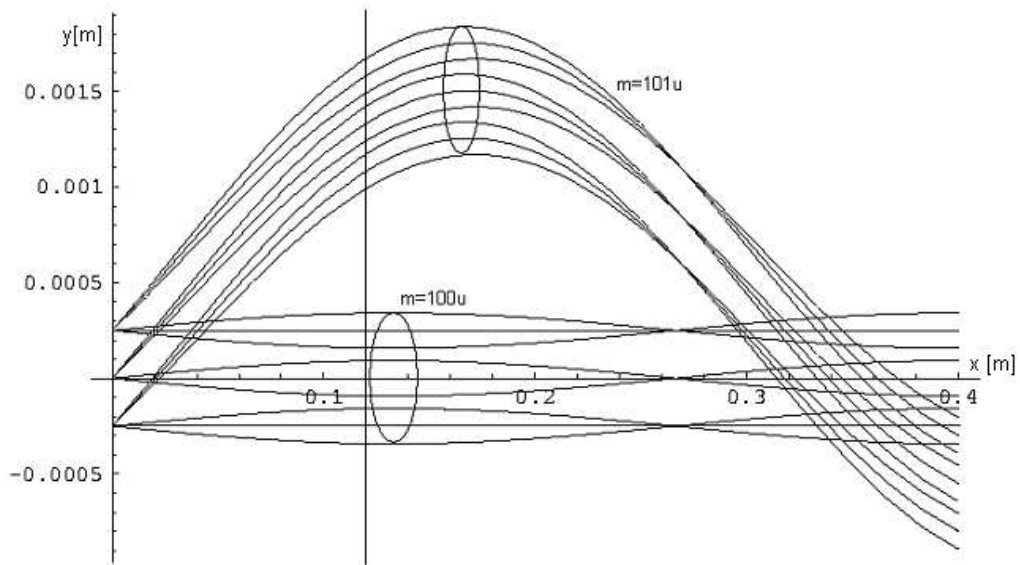


Figure 4.4: As fig 4.3. but with the beam having a finite emittance of 2π mm mrad. Separation of the two isotopes is easily possible, at the chosen filter length of 12cm.

12cm was chosen and predicts decent mass resolving power for the important region from about 20u to 100u.

Figures 4.2 to 4.6 also show another property of a Wien filter, focusing of the ion beam. Although useful for some applications this feature can be disturbing if used as a filter. The position of the focus depends on the ion and filter properties and cannot be changed for constant mass and energy. If the focus is somewhere between the filter and the detector, the beam diameter increases again before the beam reaches the detector, and mass separation may become impossible.

Furthermore, even unlikely, it is always possible that for a combination of two ions with different masses, both make it through the separating slit. The first one moves straight through and the second one, because the Wien filter is focusing it back to the same point.

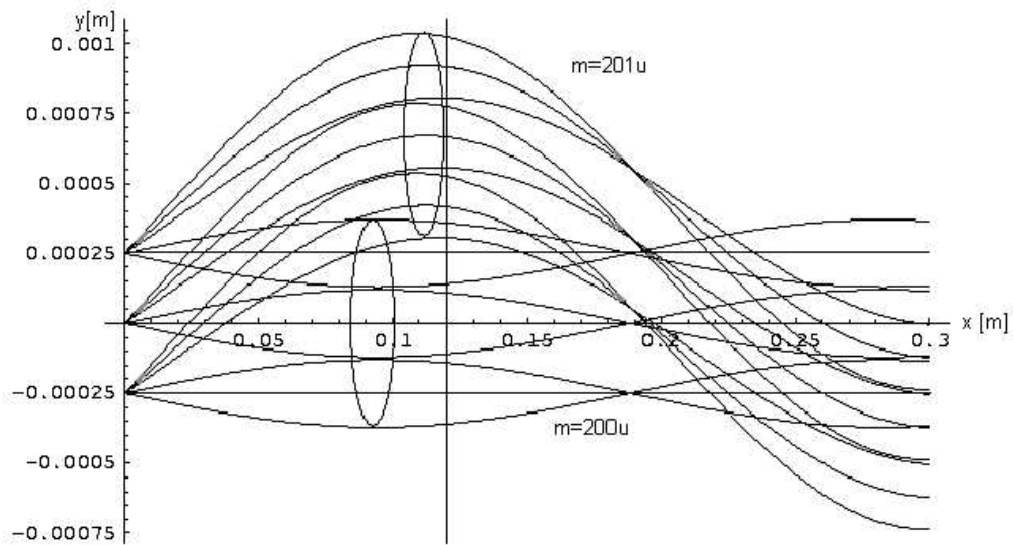


Figure 4.5: As fig. 4.4 but for masses 200u and 201u. The two masses can be separated by a slit with a width of less than 0.5mm.

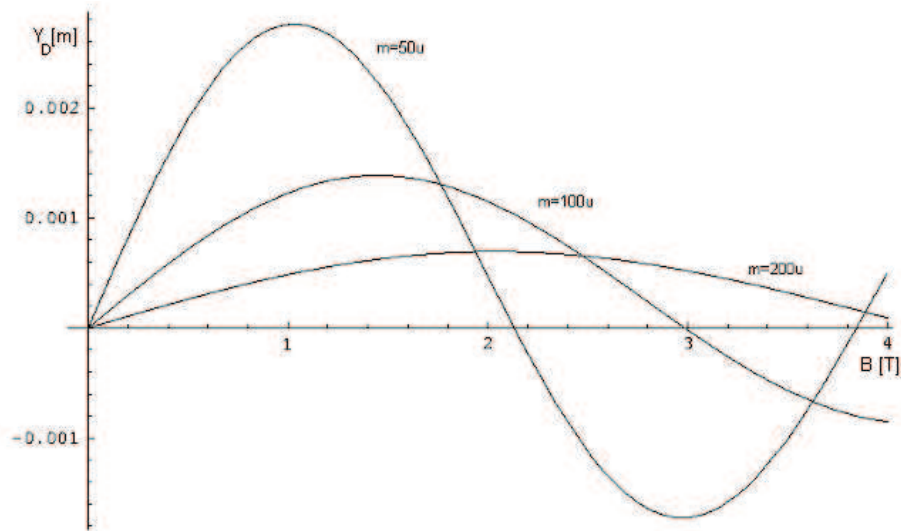


Figure 4.6: B dependent displacement for a filter with $x=L=12\text{cm}$, $D=20\text{cm}$, $K=5\text{keV}$ for three selected mass pairs.

4.2 Realization of the Wien filter

According to equation 4.5 it is necessary to have a constant ratio B/E to achieve a straight path for a desired mass. To realize this, the electric field needs to match the magnetic field. Therefore the magnetic field structure along the ions path needs to be known. As a first step towards the construction of the filter, the magnetic field was simulated. For this purpose a filter configuration as shown in fig. 4.7 was chosen.

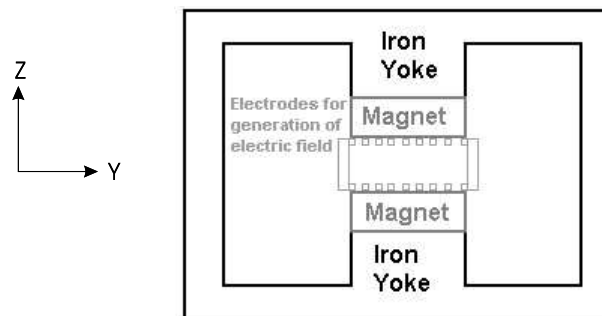


Figure 4.7: Simplified layout of the Wien filter.

The permanent magnets create the north and south poles of the filter. The magnets are attached inside an iron yoke. The yoke is used to shape and strengthen the magnetic field.

4.2.1 The magnetic field

In order to make realistic ion trajectory calculations possible, the magnetic field needs to be determined first. For the simulation of the field the PANDIRA code was used, which is included in the Poisson Superfish code package [17]. It solves a generalized integral form of Poisson's equation in two-dimensional Cartesian coordinates and is the only code that can calculate the magnetic field for permanent magnets. The result is based on the coercitive force and residual induction of the magnet used.

The PANDIRA code can only handle two dimensions, while three dimensions are required for the ion trajectory simulations. In order to deal with this limit of the code, the simulations were split in one for a y - z plane and one for a x - z plane. The simulation in the y - z plane was used to determine

the shape of the yoke. The simulation in the x-z plane was used to determine the fringe fields along the axis of the filter.

Fig. 4.8 shows the yoke shape used for the simulation. It is close to the final LEBIT design.

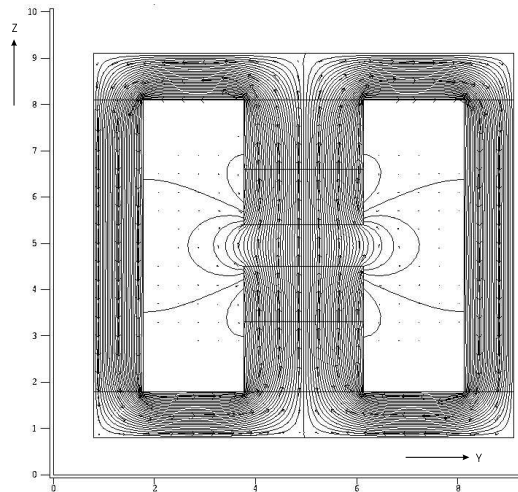


Figure 4.8: Result of a PANDIRA simulation of the magnetic field in the y-z plane. The simulation assumes that the extend of the simulation in the third dimension is infinite.

For the simulation of the field in the x-z plane a trick was used. Since PANDIRA is lacking a third dimension the yoke can not be closed in the y-z plane as it should be. Instead it is closed in a wide loop, as shown in fig. 4.10. In order to get a good approximation for the fringe field.

A comparison of the simulations for the fields in the x-z plane and the y-z plane shows that the peak values of the fields are not the same. The reason for the disagreement is the amount of permanent magnetic material implemented in both simulations and fringe effects. PANDIRA is assuming that the third dimension extends to infinity. Therefore, and because of the fringe field effects, the simulation for the field in the y-z plane is more accurate in terms of total field strength.

For the ion trajectory simulation the effect of the fringe field of the x direction is more important. Therefore, the simulation for the x-z plane will

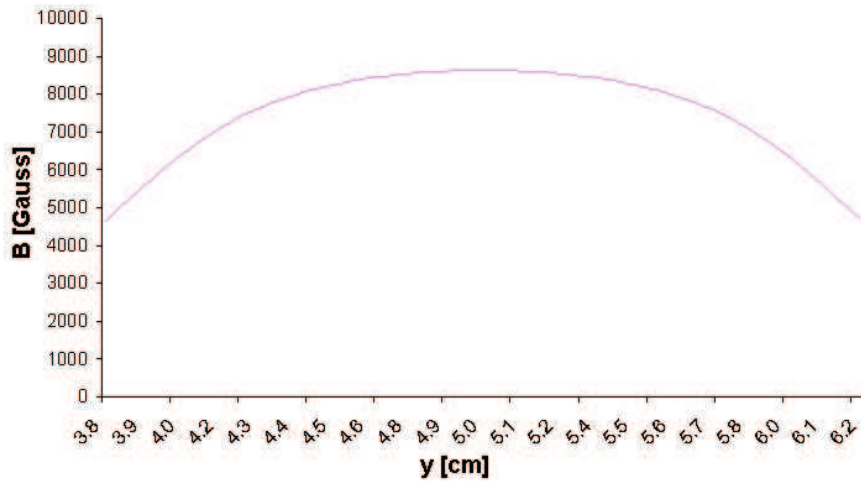


Figure 4.9: Magnetic field strength along the symmetry line in the y-z plane. B is almost homogenous in the center and has a peak value of 0.863T

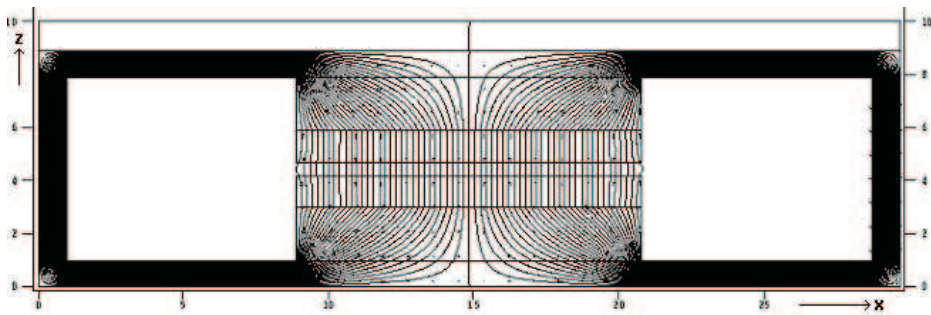


Figure 4.10: Magnetic field lines of the longitudinal field in x-z dimension as simulated with PANDIRA

be used for this purpose

Drawing equation 4.18 with the simulated magnetic field strength of $B=0.924\text{T}$, leads to fig. 4.12. It can be seen, that a mass resolving power of 200 is possible for an ion beam with zero emittance.

Simulations with different yoke shapes showed that the actual shape of the yoke had almost no influence on the effective field value. Neither did the magnetic permeability of the yoke material. The most important parameter was the gap between the magnets. Fig. 4.9 shows the strength of the field in

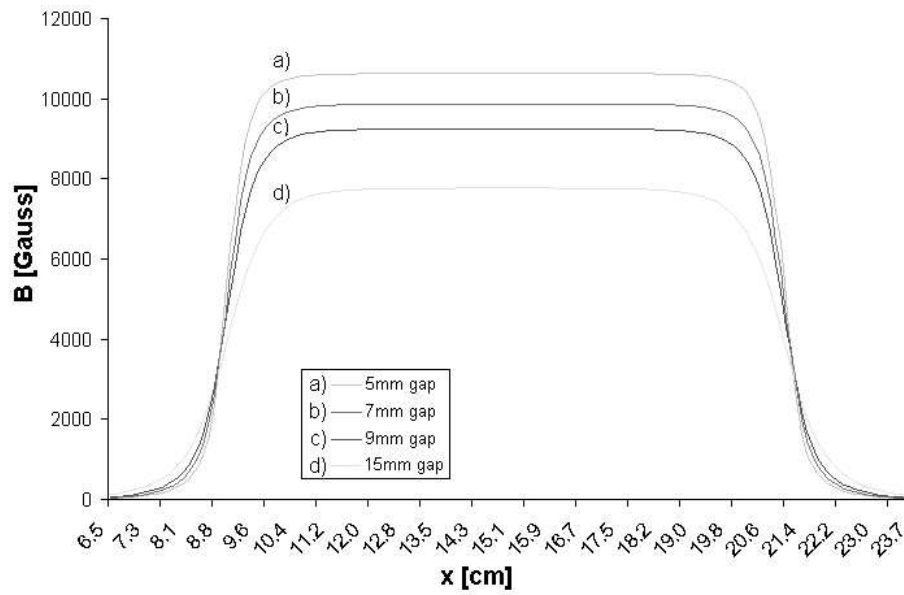


Figure 4.11: Strength of the longitudinal field along the x-axis for different gaps between the magnets. The 9mm field has a maximum strength of 0.924T.

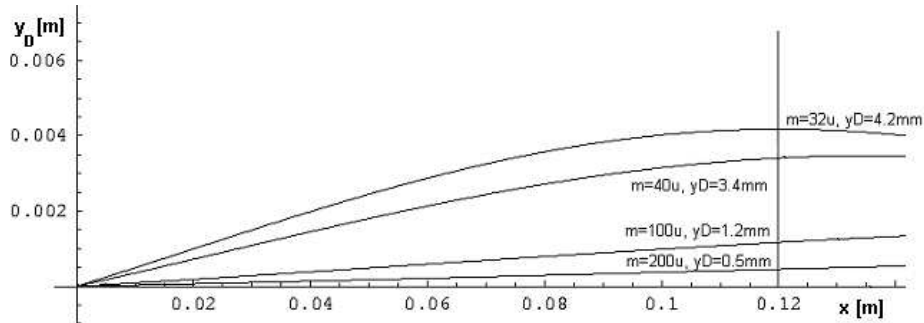


Figure 4.12: Displacement $y_D(x)$ for $B=0.924T$, and $l=20cm$. The values shown for y_D are for a filter length of $x=L=12cm$ and indicate the displacement of mass $m+1$ with respect to m .

the y-z plane with a 9mm gap. Fig. 4.11 shows field values in the x-z plane for different gap values.

4.2.2 The electric field

Since the shape of magnetic field is practically fixed, the electric field needs to be matched to the magnetic field. The magnetic field is almost constant in the y - z plane, consequently the electric field needs to be constant as well. Using a finite plate capacitor with a large ratio of plate separation to plate size gives a very inhomogeneous electric field. This problem can be corrected if the potential between the main electrodes is forced to drop linearly. For this purpose, stripe electrodes are added as shown in fig. 4.13. A resistive chain connects the stripe electrodes and creates a linear dropping potential.

Again it is necessary to look at the fields in the y - z plane and the x - z -plane separately, in order to compare it to the magnetic field.

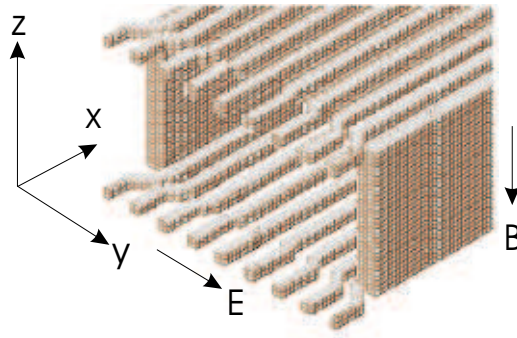


Figure 4.13: Three-dimensional image of electrode structure as used in a SIMION simulation. The small stripe electrodes between the large field electrodes are used to form a linear dropping potential and a homogeneous electric field.

The shape of the electric fringe field in the x direction has to be similar to the shape of the magnetic fringe field. Fig. 4.14 compares an unmodified electric field generated by a plate capacitor and nine stripe electrodes with the demanded electric field. It is easy to see that the electric field strength needs to be reduced towards the end. As a first measure the length of the plate electrodes is reduced weakening the field strength at the end. Secondly, the distance between the stripe electrodes is increased at both ends, as shown in fig. 4.13. Finally, grounded shielding electrodes in front and behind the filter modify the field and achieve the result shown in fig. 4.15. A suitable

configuration was found with the following parameters: 118mm long stripe electrodes and 108mm long main electrodes. The two metal shields in front and behind the filter are located 6mm in front of the stripe electrodes. The holes in the shielding plates are 6mm high and 18mm wide.

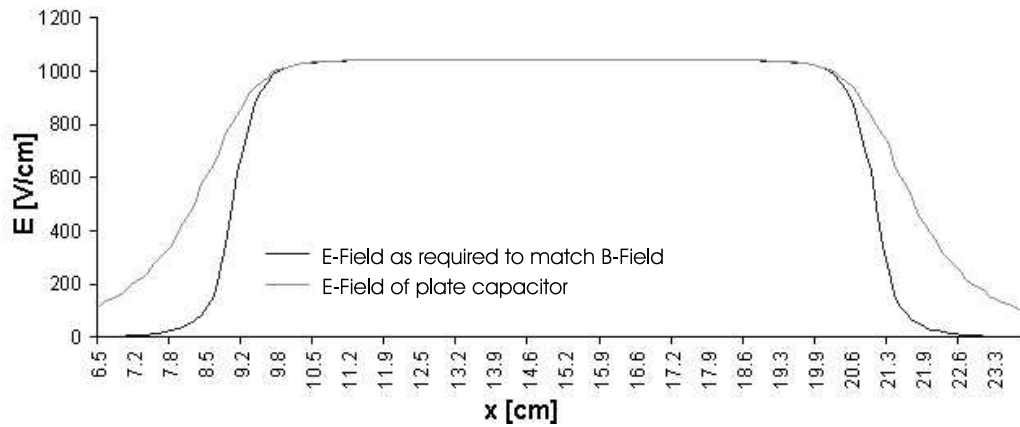


Figure 4.14: The longitudinal electric field of a plate capacitor including nine stripe electrodes compared to the electric field as it should be in order to match the shape of the magnetic field strength.

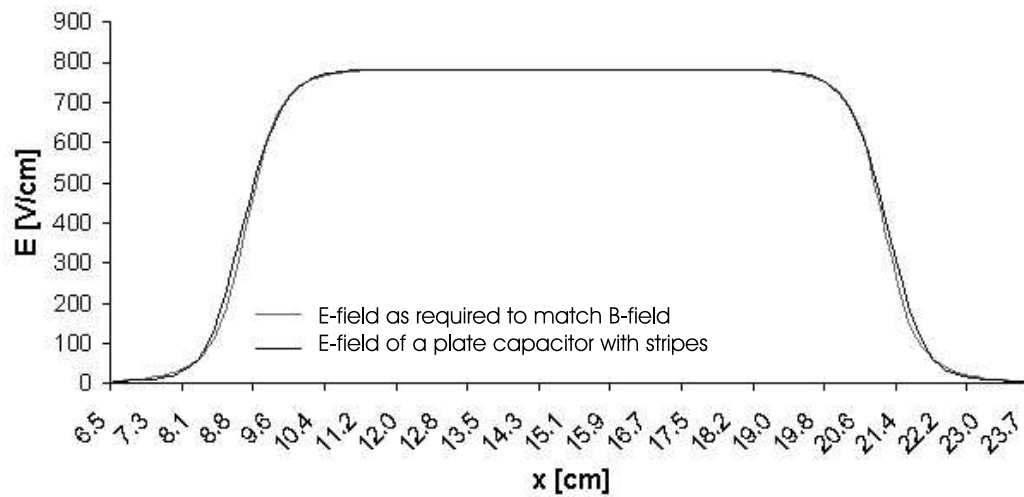


Figure 4.15: Electric field using stripe electrodes and guard electrodes compared to the field as required to match the magnetic field.

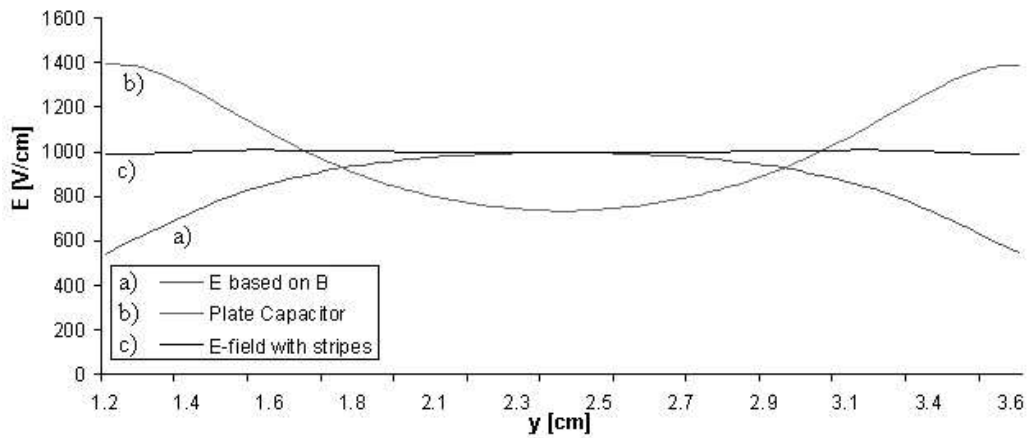


Figure 4.16: The electric field of a plate capacitor is compared to the electric field using the nine stripe electrodes and to the demanded electric field based on the magnetic field strength.

Fig. 4.16 shows the electric field strength in the y - z plane of a plain plate capacitor and one with the stripe electrodes added. Both are compared to the desired electric field strength based on the magnetic field strength. According to fig. 4.16, 95% agreement is given at $\pm 4.8\text{mm}$ around the center when using constant potential differences between the stripe electrodes. If the potential differences are not kept constant, but adjusted, perfect agreement can be achieved. For the purpose of this Wien filter, the linear potential has sufficient accuracy in the required region.

To realize a linear potential change an infinite number of stripe electrodes would be advantageous. For a finite number, the potential shows steps that become more pronounced for increasing distance from the symmetry axis towards the stripe electrodes. Figures 4.17 and 4.18 show the electric field strength in the y - z plane for different gap sizes and offset from the symmetry axis in the z direction. The off-axis values for the electric field strength are divided by those along the symmetry axis for easier comparison.

According to fig. 4.17, a step of 1mm in the z direction leads to almost no change in the electric field. An increase to 2mm starts showing the effect of the electrode configuration. The difference between 2mm off-axis and on axis is less than 1%.

Going 3mm off axis the inhomogeneities of the field are less than 5%. Fig.

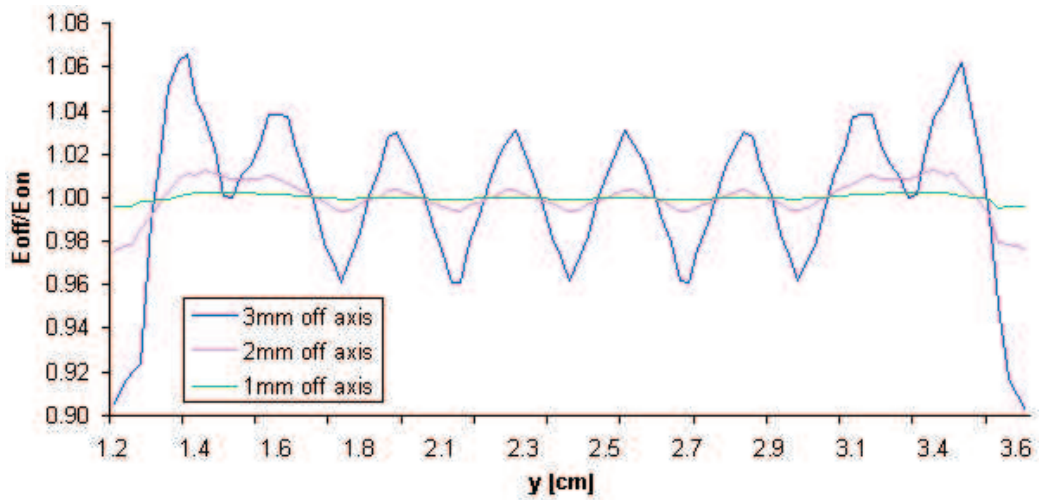


Figure 4.17: Ratio of the electric field strength off-axis (E_{off}) to the one on-axis (E_{on}) for a 9mm gap between the top and bottom stripe electrodes.

4.18 shows the same for a gap of 5mm between the top and bottom stripe electrodes. The smaller gap is necessary since the first electrode structure is milled out of 2mm thick circuit boards, which reduces the gap. Fig. 4.18 indicates that 1mm off axis does not lead to electric field inhomogeneities larger than 1%, 1.5mm off axis leads to inhomogeneities of about 5%, while 2mm off axis has an error of 20% to 30%. Assuming an emittance after the

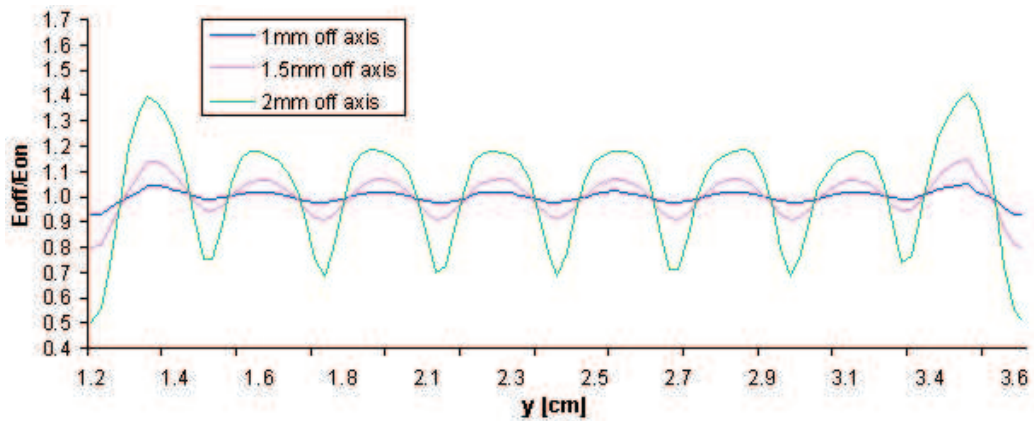


Figure 4.18: As fig. 4.17 for a 5mm gap.

Table 4.1: Comparison between calculated and simulated displacement values, for $K=5\text{keV}$, $D=20\text{cm}$ and $x=L=12\text{cm}$

Mass	Theory	Simulation
32	4.15mm	4.55mm
40	3.41mm	3.60mm
100	1.17mm	1.20mm
200	0.46mm	0.46mm

source of 2π mm mrad and a 0.5mm exit hole in the source anode the opening angle after the source should be 4π mrad. The emittance can be improved by reducing the beam diameter with a diaphragm. In the worst case it leads to an opening of the beam after the filter of about 1.5mm depending on how far the source is in front of the Wien filter.

4.2.3 Ion trajectory simulation and mass resolving power

In order to evaluate the expected mass resolving power the magnetic and electric field have been combined in ion trajectory simulations with SIMION. The simulations serve two purposes. They allow for a comparison of the theoretical results for the ideal Wien filter with the simulation and for a comparison of the simulation with the measurement. The result for the magnetic field in the x-z plane is used. Due to the two dimension limit of the simulation, it is homogenous in the y-direction.

The values used for the theoretical calculation used in chapter 4.1 and those finally used in the measurement differ in the distance D after the Wien filter. A value of 20cm was used in the previous chapter, and is used in this chapter for the comparison of simulation and calculation. For the first measurements a distance of 50cm is used.

The first simulations use the same values as the calculations shown in fig. 4.12. Table 4.1 compares them to the corresponding simulation. Theory and simulation are in very good agreement for high masses. For low masses a deviation of up to 10% is observed. To understand this, a second look at fig. 4.6 is helpful. The figure shows, that for very low magnetic field strength relatively large displacement is obtained for light ions. In the theoretical calculations a magnetic field of exactly 12cm was assumed, the simulation takes the fringe field into account, which increases the effective filter length.

The fringe field is small and has less impact on higher masses. There is no single value for the effective length that can fit the calculation to the simulation.

The simulation has been used to determine the expected mass resolution. Ions with an emittance of 2π mm mrad are stopped at a 1mm wide slit 20 cm behind the filter. With this boundary conditions simulations were performed for different mass ranges. The largest pair of neighboring masses that can be completely separated is 82 and 83, as shown in fig. 4.19. This indicates a mass resolving power $R = \frac{m}{\Delta m}$ of about 80.

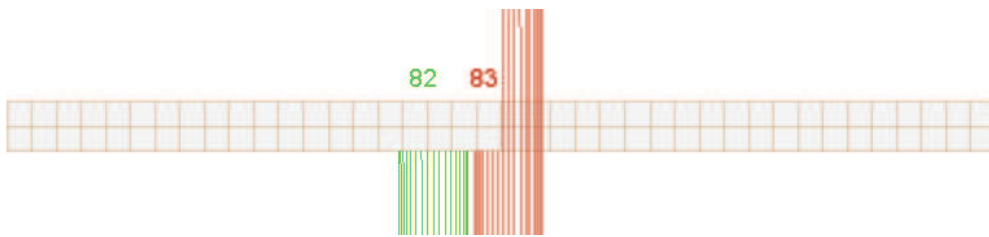


Figure 4.19: Simulation of the mass separation for $A \approx 80$ ions with $K=5$ keV. The grid has a slit of 1mm and is placed 20cm behind the filter. Two grid boxes correspond to 1mm.

Fig. 4.20 shows the result for Argon. The difference to fig. 4.19 is that D was increased to 50cm as it was realized in a latter measurement. The three stable Argon isotopes can be very well separated.

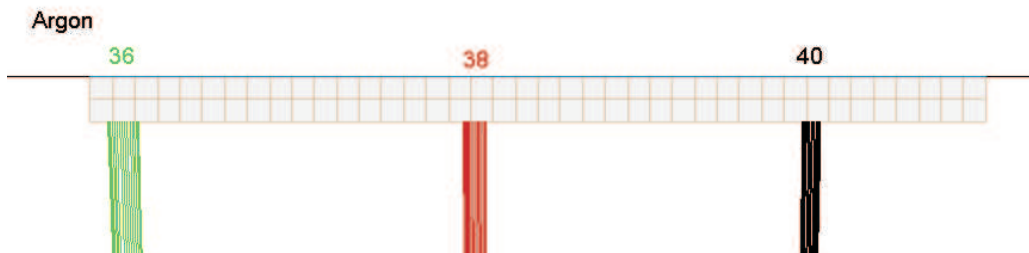


Figure 4.20: Simulation for Argon under same conditions like the experiment. $K=5$ keV, $x=L=12$ cm, $D=50$ cm. The grid is the same as in the fig. 4.19

4.2.4 Construction

The design was based on the calculation and simulations for the Wien filter. A list of parameters for the LEBIT Wien filter is given in table 4.2. Fig. 4.21 shows a 3 dimensional technical drawing of the filter, while pictures of the completed device are shown in fig. 4.22 and 4.23. The magnets used are sintered neodymium-iron-boron (Nd-Fe-B) magnets manufactured by Stanford Magnets Company. They are a custom made version of model N45 with a residual induction B_r of 1.32T-1.38T and a coercive force H_c of 11.0kOe=875.82kA/m. They are nickel coated in order to reduce outgasing.

The stripe electrode structures for the generation of the electric field are made by milling the required structure out of 2mm thick copper circuit boards. The main electrodes are manufactured out of aluminium using an arrangement that allows tightening of the upper half of the electrode against the lower part so that it will fit tightly in any situation. The stripe electrodes are connected to eight 5W, 2M Ω resistors using capton coated copper wires. The resistors are arranged on a Teflon board.

Table 4.2: Mechanical properties of the LEBIT Wien filter.

Length	120mm
Gap between magnets	9mm
Length of single magnet	40mm
Width of single magnet	24mm
Gap between stripe electrodes	5mm

For initial testing, the gap between the magnets was increased to 11mm for two reasons. The effect of the inhomogeneous vertical transversal field would be reduced and the magnetic field would be weaker, in turn also requiring a less strong electric field. The latter allowed reducing the voltage applied to the system what was important since high voltage power supplies were not available at the time.

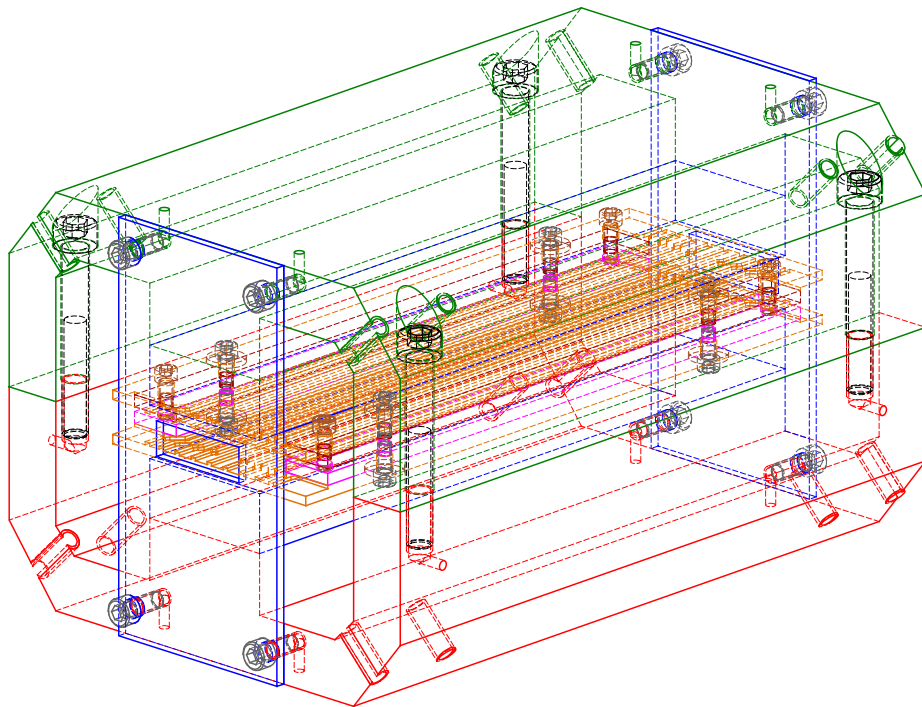


Figure 4.21: Wire frame drawing of the Wien filter, including stripe electrode structure and metal guards at front and backside of the filter.

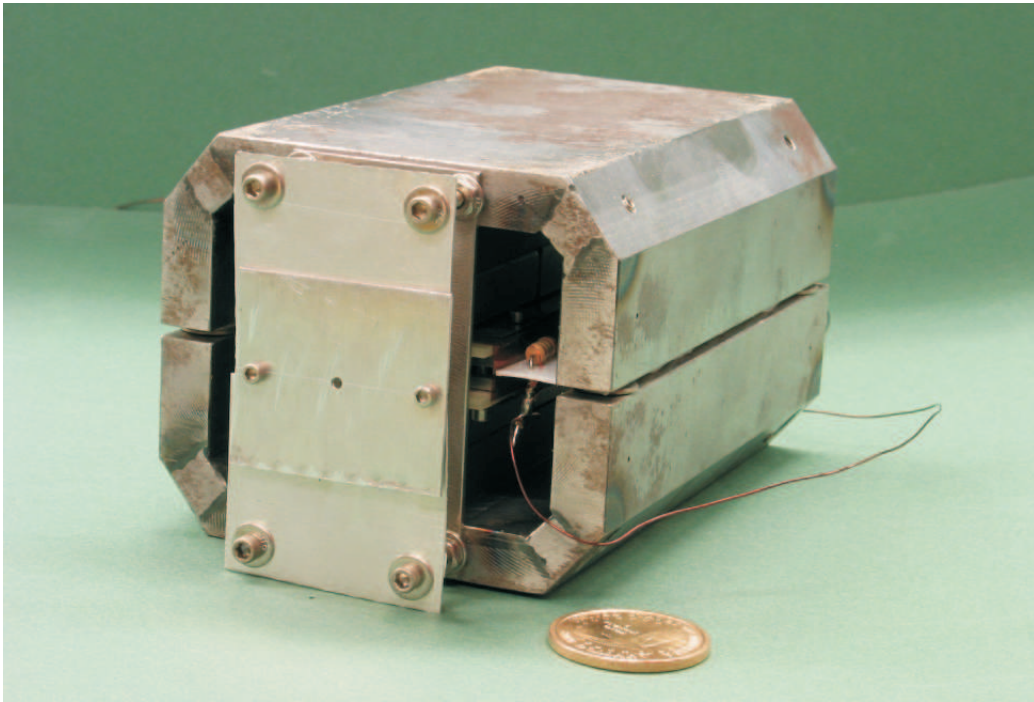


Figure 4.22: Picture of the Wien filter back side. The iris that limits the beam to a 2mm diameter can be clearly seen. Also one resistor from the resistive chain is visible.

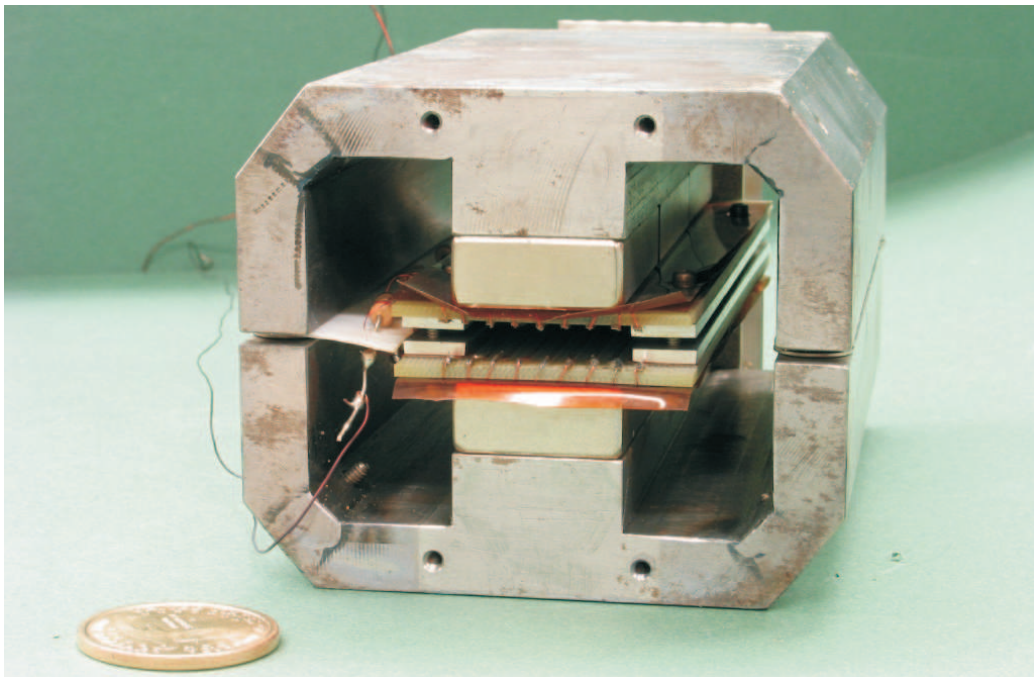


Figure 4.23: Metal shield has been removed from the front of the Wien filter. The electrode structure and magnets are visible.

4.3 Results of test measurements

4.3.1 Magnetic field

The goal of the first measurement was to determine the magnetic field. For this purpose a transversal hall probe was used. Fig. 4.24 shows the results of such measurements for a 9mm and a 11mm gap, compared to the magnetic field simulation for the 9mm gap.

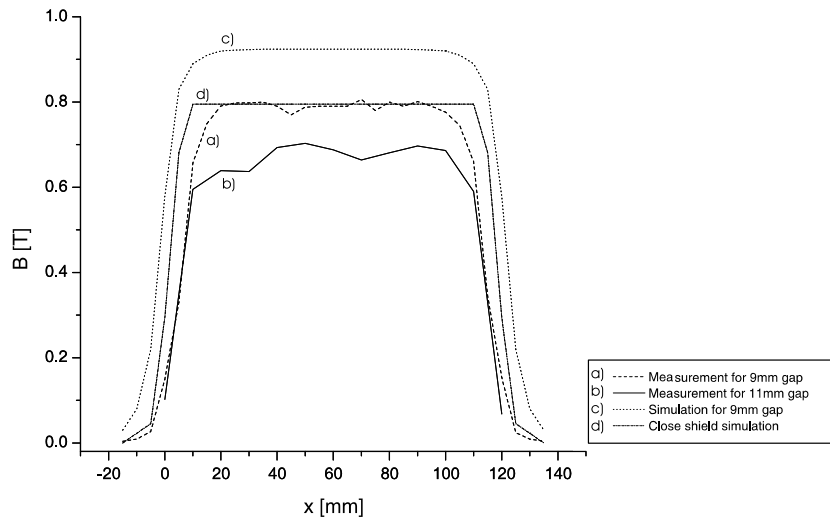


Figure 4.24: Measurement of the magnetic field for a 9mm and 11mm gap between the magnets compared to the simulation for 9mm. The faster decrease is partially countered by moving the metal shields closer, as shown in the close shield simulation. The errors of the measurement are in the order of 200G.

The measurement shows two effects. The magnetic field strength is lower than expected from the simulations and decreases faster. This result is not too surprising considering the simplified assumption made in the simulation.

In order to counteract the faster decrease the electric field guards are moved closer to the magnets. This change is shown in the normalized close shield simulation as seen in fig. 4.24. Normalized, because the maximum value is normalized to the magnetic field strength of the 11mm gap measurement.

From fig. 4.6 can be seen that for small magnetic fields, the sinusoidal function can be approximated by a linear function. This allows a linear correction factor to be introduced that accounts for the smaller magnetic field. This factor is obtained by determining the average ratio of simulated to measured magnetic field. For the 9mm gap a correction factor of $c_{9mm}=0.858\pm 0.024$ is obtained. For the 11mm gap a value of $c_{11mm}=0.696\pm 0.027$ is determined. Those factors are used to get an idea where to look for peaks.

4.3.2 Temperature Dependence

For the measurement, the ion source is set up as explained earlier. The Wien filter is placed 5mm after the 2mm iris behind the acceleration electrode. An additional 2mm iris is added about 1cm behind the Wien filter. It is used to stop any ions that would exit the filter far off axis, and also limits the beam size.

50cm behind the filter, an ion detector is installed. This detector was simply a 1mm wide strip of metal, mounted in an insulated way and connected to a vacuum feedthrough. The signal was fed into a logarithmic amplifier. The output of this amplifier is then recorded by the control system.

To scan over a specific mass region, the voltage applied to the Wien filter was varied and the ion current was measured. The mass is related to the voltage in the following way:

$$m = 2Kd^2 \frac{B^2}{U^2} \quad (4.20)$$

Where $d=24\text{mm}$ is the distance between the main electrodes.

A logarithmic amplifier, is used to measure the ion current.

First measurements with the Wien filter showed an interesting effect illustrated in fig. 4.25. The figure shows repeated mass scans with the filter. It can be seen, that peaks shift their position from measurement to measurement. Careful consideration of all possible reasons led to the conclusion that the Wien filter shows a temperature dependence.

To get an idea of the temperature at the Wien filter, a PT100 gauge was installed next to it inside the vacuum. It was first assumed that the temperature will not raise very much. However, measurement showed that the ion source heats the Wien filter up to over 70° Celsius. For most magnets this would not pose a problem, however Neodym based magnets have a low

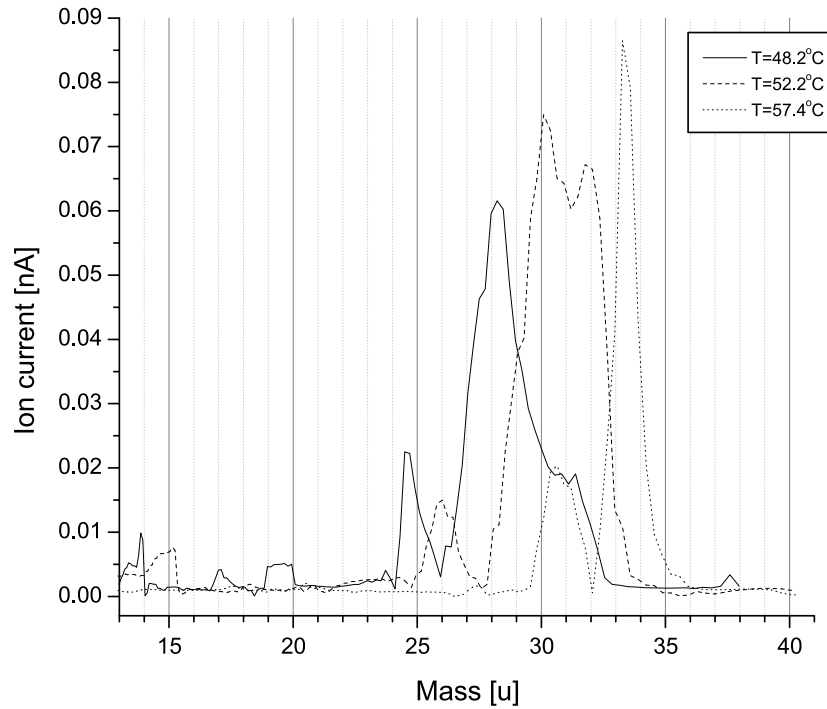


Figure 4.25: Illustration of the temperature dependent filter operation. For raising temperature the magnetic field decreases and the Nitrogen peak shifts to higher masses.

Curie temperature [18] of only 80° Celsius [19]. Therefore the assumption of a temperature dependance for the magnetic field was very reasonable.

A theoretical solution for the temperature dependant saturation magnetization can be found by using a mean field approximation in combination with the Brillouin expression for the magnetization [20]. The resulting equation can be solved graphically and leads to a temperature dependance similar to the one shown in fig. 4.26, for Nickel.

At room temperature (293K) the magnetic field has a measured strength of about $\tilde{0}.69\text{T}$. Assuming the curve for Nickel to determine the temperature dependance of the magnet, the magnetic field strength would decrease to $\tilde{0}.53\text{T}$ for 313K. That is a change of 8mT/K .

The measured change at operating temperatures of $300\text{K}\pm 10\text{K}$ is 5mT/K corresponding to a change of approximately $0.78\%/K$ which leads to a shift

of $0.5\mu\text{K}$ on the mass scale.

Considering that the theory gives only a very rough approximation for Nd-Fe-B it is in very good agreement with measurement and supports the idea that a temperature dependence is responsible for the observed results.

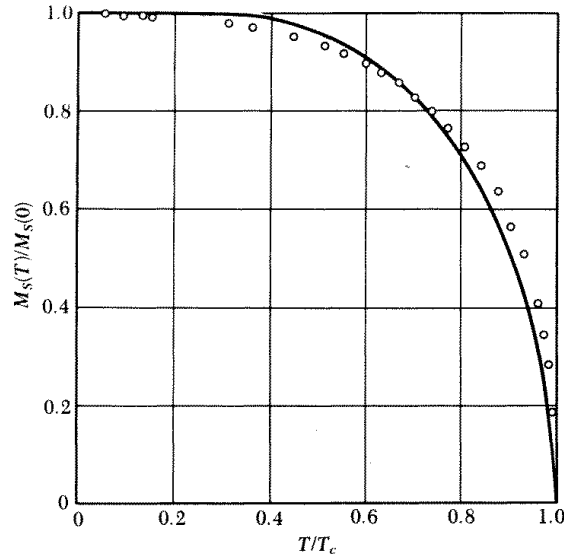


Figure 4.26: Measurement of temperature dependent saturation magnetization of Nickel and theoretical curve based on mean field theory for spin 1/2 ions. [20]

To provide a more stable and colder environment for the Wien filter a huge heat sink, as seen in fig. 3.1, was installed at the Wien filter cross and water cooling was added to the ground potential part of the ion source. This sink decreased the maximum temperature from over 70°C to under 40°C .

4.3.3 Mass resolving power

The definition given for mass resolving power in subchapter 4.1 is perfect for a square isotope distribution. To determine the mass resolving power for a gaussian distribution, the **full width at half maximum** (FWHM) is used.

$$R = \frac{\text{mass}}{\text{FWHM}}$$

Several measurements were performed of which two will be discussed here. One measurement was performed with ^{40}Ar at an ion energy of 5keV and the other with $^{28}\text{N}_2$ ions at 1.5keV.

Based on the discussion in chapter 4.1. for an emittance of 2π mm mrad the theoretically expected resolution for square distribution should be 50 for 5keV if the ions are detected 50cm behind the Wien filter.

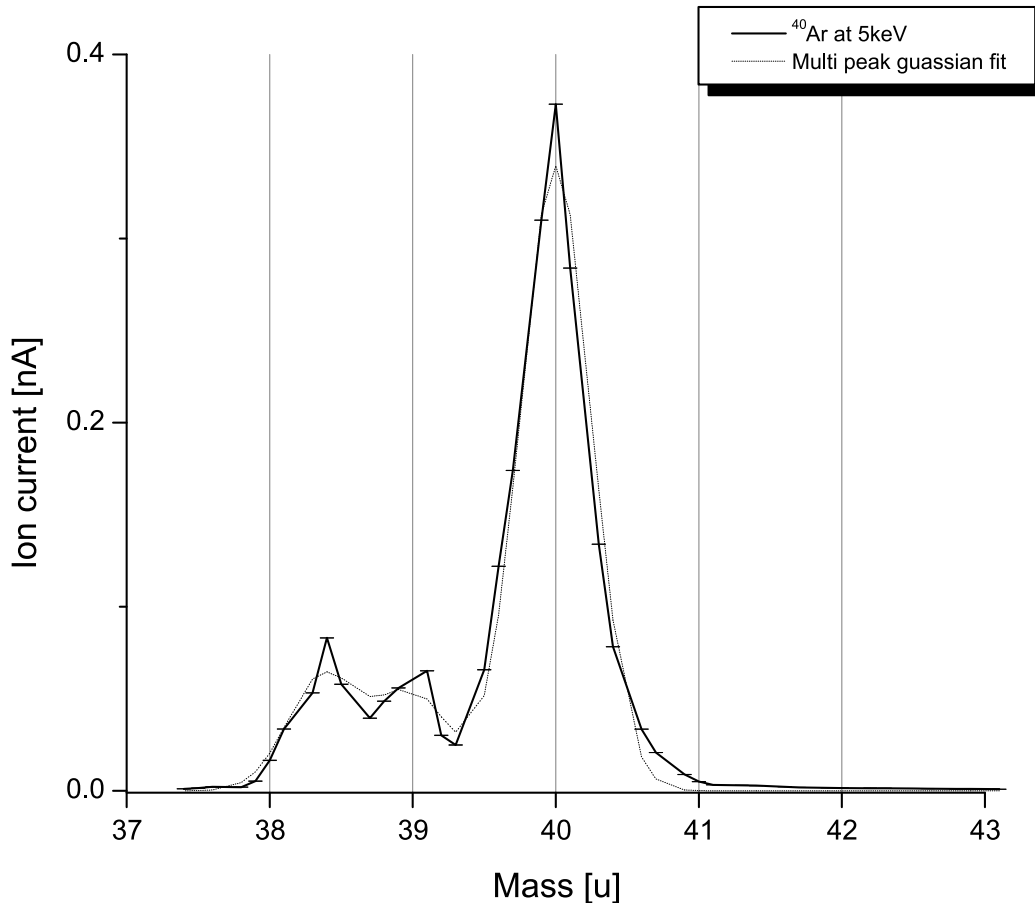


Figure 4.27: Measurement of mass resolving with Argon for 5keV beam energy. FWHM mass resolving power is 41.6 ± 1.0

Fig. 4.27 shows the result of the measurement for Argon. The measurement has a good statistic and was performed under constant pressure at the Wien filter. The temperature was monitored over the time of the measure-

ment and the observed change corresponded to a magnetic field change of less than 1%. Fitting multiple Gaussians to the observed curve gives a mass resolving power of 41.6 ± 1.0 at 5keV, including statistical error.

This is smaller than the expected value of 50. A number of reasons could be responsible for the decrease in resolving power. First the temperature change could cause an increase in peak width. But a change in the magnetic field of $\tilde{1}\%$ from first to last scan is not enough to explain it.

Another problem related to the Wien filter is construction are inhomogeneities in the electric field as shown in fig. 4.18. From this figure it can be seen that effects from inhomogeneities should be smaller than 1% for a 2mm beam diameter.

A third reason, at least for the first measurements performed, could have been collisions of the ions with residual gas atoms. The pressure was measured far away from the Wien filter ($p=1 \cdot 10^{-6}$ mbar) and it is significantly higher closer to the source, therefore ion scattering could have been a problem. For the results shown here this was prevented by an additional turbo pump and a Penning gauge installed very close to the Wien filter. Using this gauge the pressure at the Wien filter was determined to $1 \cdot 10^{-7}$ mbar.

A spread in kinetic energy of the ions in the order of 100eV for the 5keV beam would lead to a sufficient increase in the peak width to explain the results. According to the manufacturer the ion source, should have an energy spread of 0.11eV. This has not been verified but it is very unlikely that the source would have an energy spread of 100eV.

Furthermore a systematic drift of the voltage applied to the Wien filter could cause an increase in peak width. The power supplies are equipped with a voltmeter that gives a frequently updated read back. The readout showed no unexpected behavior.

The resolving power for Argon could be explained if an emittance of 10π mm mrad is assumed for the ions delivered by the source. That led to an expected resolving power of 41.5.

The theoretical mass resolving power for ion energies of 1.5keV is 93 assuming an emittance of the ion beam after the source of 2π mm mrad. The Argon measurement however suggests that the emittance is 10π mm mrad. If this is used to recalculate the resolving power for 1.5keV, the Nitrogen measurement should lead to a resolving power of 78.

The result of the N_2 measurement is shown in fig. 4.28. From the width of the $A=28$ peak a resolving power of 59.0 ± 4.5 including statistical error

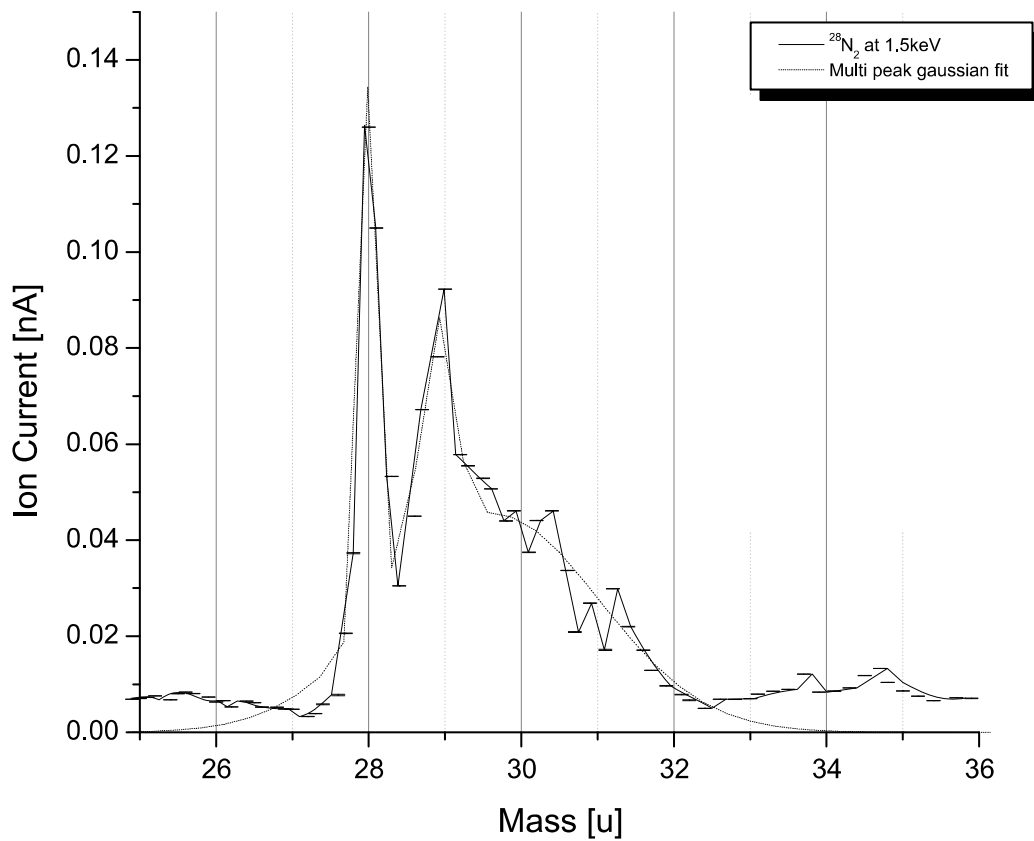


Figure 4.28: Measurement of mass resolving with Nitrogen for 1.5keV beam energy. FWHM mass resolving power is 59.0 ± 4.5

is obtained. The error is larger than in the case of Argon, since fewer scans were made for Nitrogen.

The mass spectra and peak shape demand a more detailed discussion. The peak assigned to mass 28 is really sharp but followed by other structures towards heavier masses. The easiest explanation would be that the ion source delivered many masses in this mass range. However there are very few molecules and elements that have the necessary charge-to-mass ratio. NO would be a candidate for mass 30 but its production is quite unlikely and does not explain all the other peaks. To find a molecule that fits mass 29 is even more challenging and the possible explanations are very unlikely.

That makes it reasonable to look for aperitive effects. For Nitrogen two

problems show up. Firstly, the ion source functions poorly if used with air or Nitrogen. It needs to be operated at high gas pressures (about one to two orders of magnitude higher than with Argon), high filament current and high anode voltage in order to get an ion current that is still an order of magnitude lower than the currents achieved with Argon. Measurements at different gas pressures indicated that the peak width and height depend strongly on the actual pressure. For the measurement shown in fig. 4.28 it was attempted to keep the pressure as constant as possible, but fluctuations could not be eliminated completely. Measurement with the microchannel plate detector (as described later) showed indeed that intensity and beam size changed as a function of time if the source is operated with Nitrogen.

A second problem with Nitrogen lies in the ion trajectory. A mass 28 beam is already focused between the filter and the detector, so that the beam spot gets bigger with increasing distance. Theory also shows, that for 1.5keV beam energy, neighboring masses between 15 and 27 cannot be distinguished. Masses in this region exit the Wien filter at a positive y position, but with negative slope and hit the detector together with its neighbor masses. Below mass 15 the displacement is large enough again to separate the masses. If this effect would affect the quality of the measurement with Nitrogen, an increase in beam energy should solve the problem. However, measurement showed very similar problems at higher energies, which indicates that more systematic studies are still required.

The theoretical expectation can be fitted to the measurement if an emittance of 16π mm mrad is used. This is larger than the emittance calculated to fit the results of the Argon measurement, what is not completely surprising, since it was expected that the emittance increases with decreasing beam energy. An increase of 60% however is unlikely.

The exact reason for the low resolving power is not completely understood yet. The ion source is definitely not behaving as expected. More detailed studies of the ion sources behavior could help to solve the problem. Once the source is understood completely it should be possible to achieve the calculated mass resolving power.

Chapter 5

Beam diagnostics

The beam observation system for LEBIT provides beam diagnostics along the beam line from the N4 vault to the Penning trap.

As explained in chapter 2.2, a number of Beam Observation Boxes (BOB) are distributed along the beam line. This chapter will explain the detector systems installed in each BOB.

The detectors used are double sided Faraday cups, for current measurement and microchannel plate detectors (MCP) for position sensitive beam detection. This combination allows the detector system to determine beam current and position of beams with a current in the picoampere range, whether a continuous or pulsed beam is used. Since the beam can travel from the ion source backwards, the Faraday cup is a double sided detector.

5.1 Position Sensitive MCP Detector

5.1.1 General properties

Microchannel Plates (MCP) are sensitive to ionizing particles. They were originally developed as an amplification element for image intensification devices, such as night vision goggles.

A MCP consists of a lead glass plate holding a large number of channels. The channels are normally biased at a small angle. The function of each channel is that of a charge multiplier.

MCPs have a gain of 10^4 - 10^7 coupled with ultra high time resolution in the order of <100 ps. Spatial resolution is determined by the channel dimensions

and spacings.

A convenient way to increase the gain of an MCP detector is to use them pairwise. A common arrangement is the Chevron stack as shown in fig. 5.1. The stack consists of two plates in a row, separated by a very small gap ($50\mu\text{m}$ - $150\mu\text{m}$).

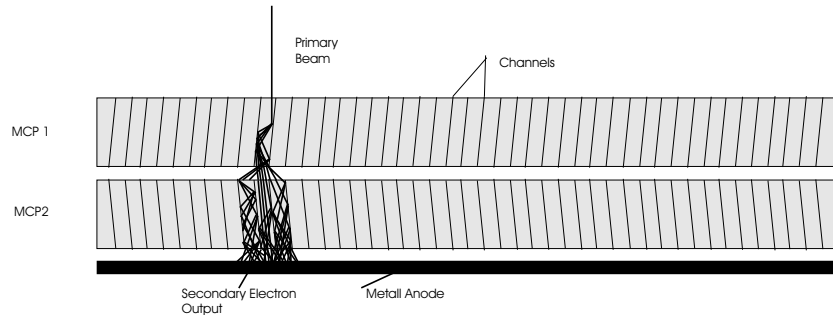


Figure 5.1: Side view of a Chevron stack of MCPs and illustration of the secondary electron amplification.

The detection efficiency for microchannel plates depends on the primary beam and varies from about 1% for photon radiation to 85% for low energy electrons and positive ions. For positive ions with 5keV kinetic energy the detection efficiency varies between 60% and 85% depending on mass and charge [21].

5.1.2 MCP detectors for LEBIT

The MCP detectors used inside the beam observation boxes are from the chevron type, combined with a phosphor screen. An incoming ion creates a shower of secondary electrons in the MCPs. The electrons are accelerated onto the phosphor screen, where the electrons create a photon beam. The beam image created on the phosphor screen was observed with a digital camera via a mirror mounted at an angle of 45° as seen in fig. 5.2. The camera itself was placed outside the beam line.

Fig 5.3 is a picture of the mounted detector array. Behind the stainless steel front plate, the MCP stack is enclosed in a Macor block. Electric contact is made with ring shaped electrodes connected to wires. They are

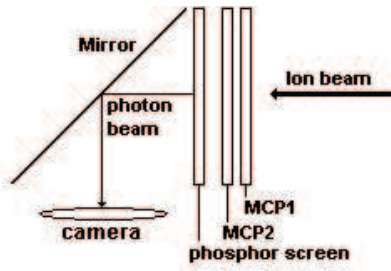


Figure 5.2: Schematics of the MCP detector system. The incoming ion beam creates a shower of secondary electrons in the MCP. These electrons are accelerated onto a phosphor screen. The beam image is observed by a camera via the 45° mirror.

connected to a flexible circuit board which is finally connected to the vacuum feedthroughs.

The capton connection provides very good flexibility and high reliability when moving the detector in and out. The detector movement is achieved by a pneumatic device, mounted outside on the flange as described in chapter 2.2.

The chosen MCP detector model is the Colutron BVS-1. Table 7.2 in Appendix of this work gives a brief summary. The detector uses a P-20 phosphor screen on an aluminized glass plate. P-20 has its peak wavelength at 560nm together with a conversion efficiency of $\eta=0.063$ photons/eV/electron.

Based on this knowledge together with a total gain $G=3.6 \cdot 10^7$ it is possible to calculate the minimum luminosity provided by a single incoming ion.

$$n_{Photons} = \eta \cdot K_{Electron} \cdot G \quad (5.1)$$

A reasonable value for the energy is about 1keV, since the electrons are slowed down by the aluminized glass plate. Therefore one incoming ion generates 2×10^9 photons. Assuming the same energy for all of the photons, the total energy can be calculated. The power can be calculated by taking into account that 90% of the energy placed in P-20 phosphor decays within 4.0ms. This results in a power of $0.2 \mu W$, which corresponds to a luminous flux of $L=0.1$ mlm. The photons will be emitted into the full solid angle. Therefore 0.7% of the photons will arrive at the camera which is 175mm away from the

detector. This reduces the luminous flux to 0.04mlux.

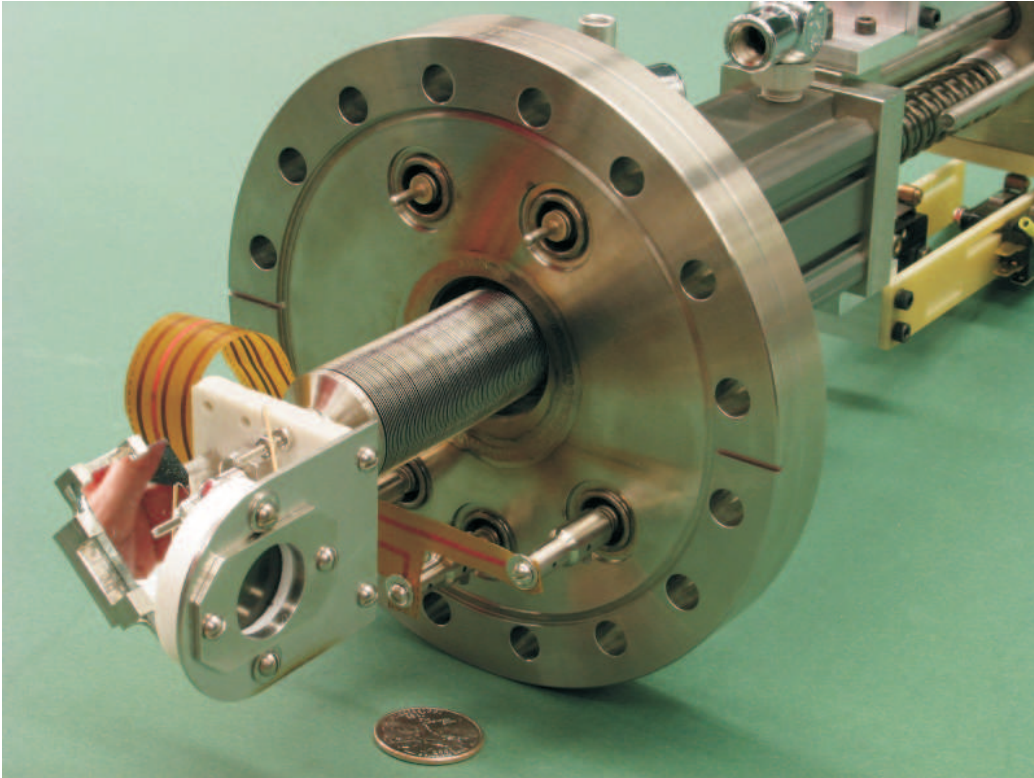


Figure 5.3: MCP detector mounted on a 6" flange. Flexible capton boards provide high voltage and signal connection. The chevron stack is encased in a Macor block mounted behind a stainless steel front plate. The mirror is necessary to observe the image on the phosphor from a perpendicular position.

High voltage for the detector is provided by HV-power supplies. Fig. 7.2, in Appendix B, shows the electronic layout used to connect the MCPs. A resistive chain of two $2M\Omega$ resistors is used as a voltage divider. The $20M\Omega$ and $47M\Omega$ resistors protect the sensitive plates and phosphor screen from damage through sparks.

The digital camera used is a Point Grey Research Firefly camera. It is capable of detecting a minimum illuminance of less than 1.0lux. Appendix table 7.1 gives a summary of more camera properties.

The camera also can be triggered. This is necessary if a pulsed beam is used. Since the phosphorescence ceases within 4.0ms the camera must take its pictures in the same time period. The camera's response to the trigger signal has been tested and found to be fast enough. The trigger signal required is a standard TTL pulse.

The camera used an IEEE1394 firewire interface to transmit data to the readout computer. Almost any camera setting can be adjusted via software.

For the first tests a variable zoom lens is used. Once the optimal lens settings are found, less expensive fixed focus lenses will be used to provide good imaging properties for all MCPs.

Fig. 5.4 shows how the camera has been mounted to the flange. The camera is operated on ground potential, while the vacuum chamber is on high voltage. PVC rods guarantee sufficient electric insulation. Since the glass viewport is larger than the lens, the rest is covered with light-tight plastic to block external light. If light is needed inside the vacuum chamber during camera operation, a lamp is connected using a fiberoptic light guide.

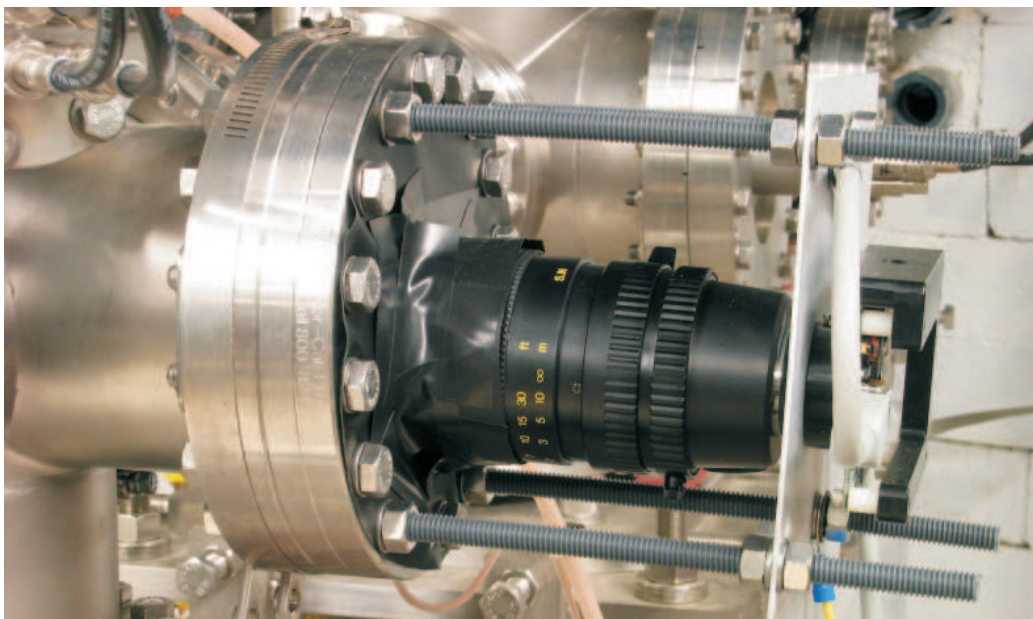


Figure 5.4: PVC rods mount the CCD camera and lens to the flange and provide insulation to keep the camera on ground potential. The glass viewport is covered with light-tight plastic.

5.1.3 MCP measurements

Several tests have been performed using the MCP detector system. Following the manufactures recommendations for the first commissioning of the MCP detectors the HV at the channel plates and the phosphor screen was raised in small steps over a long period of time until the desired voltage was reached. During the commissioning of the detector it was found that one MCP had a micro fracture. At high gain the crack emitted more electrons and became very visible. That made it impossible to operate the channel plates up to their maximum possible amplification.

For the tests involving the MCPs a beam intensity off less than 1nA was used. Fig. 5.8 shows an average beam spot. Only a low gain was necessary to make those pictures, so the effect of the crack is not visible.

The beam spot is a magnified image of the ion source exit hole, which has a diameter of 0.5mm. The spot in fig. 5.8 is approximately 1.7mm high and 1.1mm wide, what corresponds to a magnification of 3.4 or 2.2. Abberations from imperfect lens settings cause the distortions.

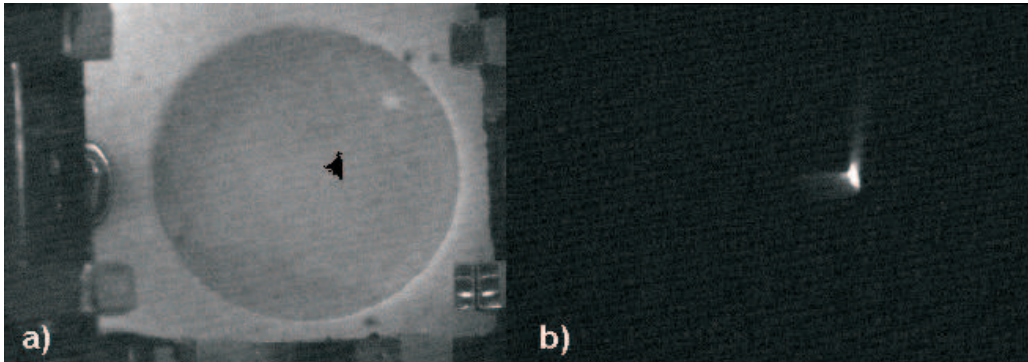


Figure 5.5: a) Combination of picture b) with an illuminated picture of the detector. b) Screen-shot of the camera readout

With better lens settings and an magnification of 1 it should be possible to image the ion sources exit hole to the phosphore screen as seen in fig. 5.6. The lens settings used to achieve this are shown in table 5.1.

Fig. 5.7 a) shows a three dimensional intensity plot of the beam spot with background subtracted. Based on the intensity information it is possible to determine the signal/background ratio to 10/1 and determine the size of the beam spot. The spot has a maximum expansion of $0.49\text{mm} \pm 0.01\text{mm}$ by

Table 5.1: Lens setting for focus in BOB3

Einzel lens after ion source	4000V
Planar Einzel lens	0V
y deflector after ion source	110V
90 degree deflector	3831V
Einzel lens before BOB3	5450V

$0.41\text{mm}\pm 0.01\text{mm}$ measured at half maximum. Slight imperfections in the lens settings or alignment of the lenses in the beam line cause some minor distortions. Nevertheless, the focus is better than expected.

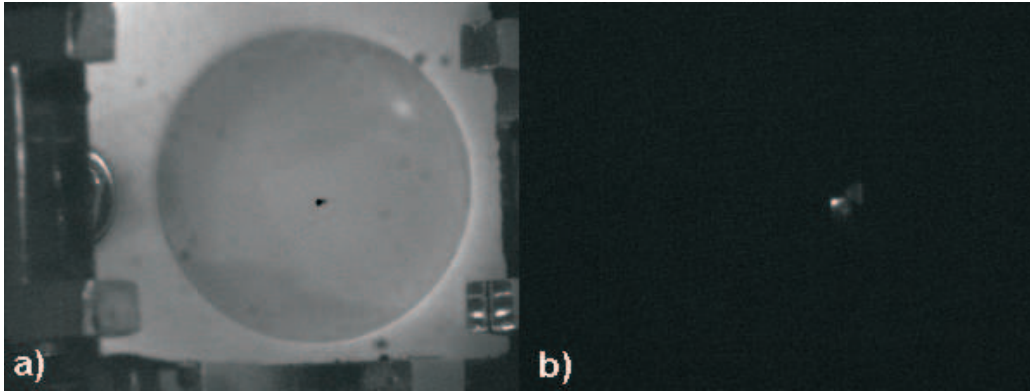


Figure 5.6: a) Combination of picture b) with an illuminated picture of the detector. b) Screen-shot of the camera readout of the focused beam.

For the third measurement, an anchor shaped negative pattern, with 0.5mm wide slits was installed 15mm in front of the MCP detector. The pattern was evenly illuminated with an unfocused beam. Fig. 5.8 shows the result of the measurement.

Based on the measurements made, it can be seen that the MCP system is working as expected. It is a very efficient tool to observe beam profiles in real-time what makes beam focusing easy.

A last measurement with a radioactive alpha particle source was heading to verify that the camera is able to see light pulses from single ions detected by the MCPs. For this test, a high intensity α -source was installed 1cm in front of the MCP detector. Half of the detector was covered with a piece of

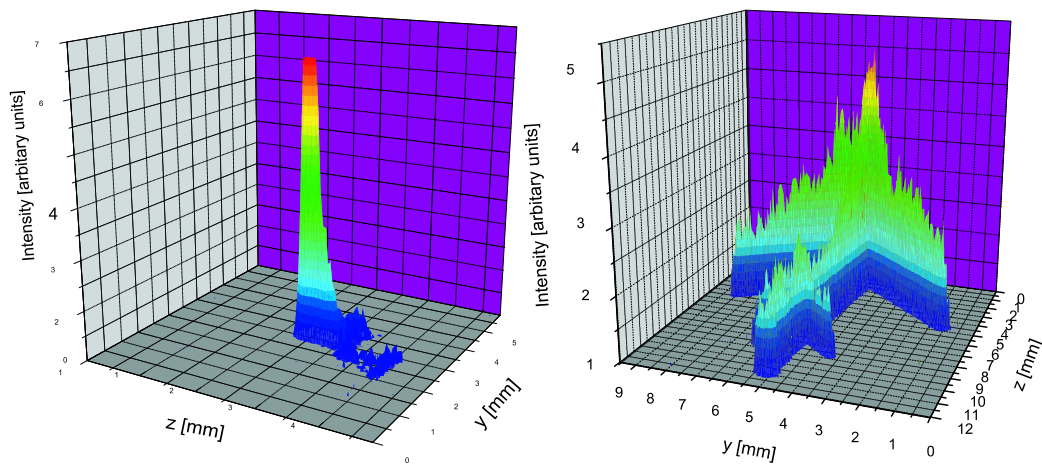


Figure 5.7: a) Plot of the focused beam spot b) Image of an anchor placed 15mm in front of the detector.

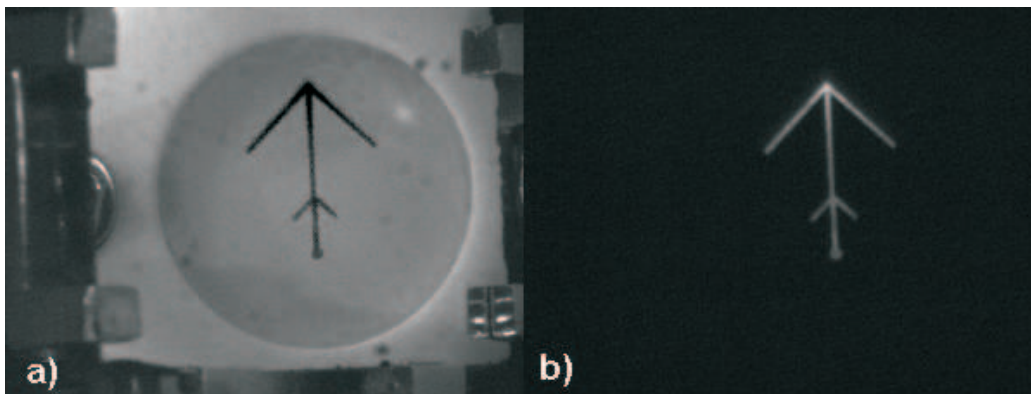


Figure 5.8: a) Combination of picture b) with an illuminated picture of the detector. b) Screen-shot of the camera readout with an anchor shaped structure in front of the MCP

sheet metal. The half covered with the metal had the crack. At high gains the crack created discharges looking very similar to the signals produced by the incoming ions. The test was not entirely conclusive, but indicated that the observation of single ions is possible.

5.2 Faraday Cup

Current measurement for the beam observation system was achieved with a Faraday cup detector. The detector has two Faraday cups mounted in opposite direction that allows the monitoring of beam coming from upstream and downstream.

Fig. 5.9 shows a schematic view of the double sided cups as used for LEBIT. The two components of each cup are the inner ion collection chamber and the suppressor ring. While the outer shell and the collection chamber are on beam potential, the suppressor is slightly below.

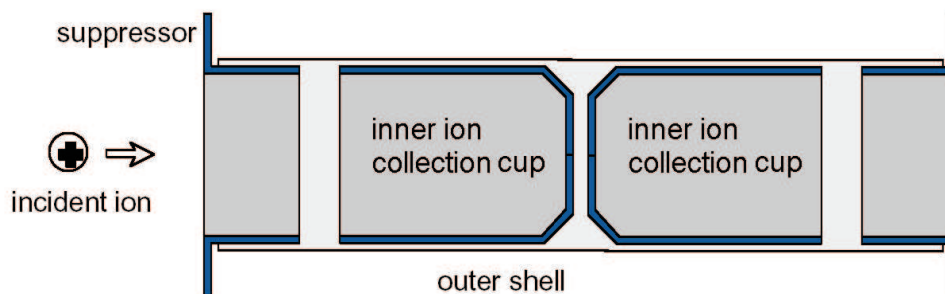


Figure 5.9: Schematics of the double Faraday cup detector. The inner cups are separated by insulators from the suppressor grids. Two sides are necessary to detect beam travelling up and down streams.

An incoming ion places a positive charge onto the collection chamber electrode. This leads to a current that is proportional to the ions charge and if the charge is known, proportional to the ions flux.

Incoming ions also create secondary electrons which could leave the Faraday cup. This additional loss of negative charge would effectively increase the measured current. To avoid this phenomenon and keep all the electrons trapped inside the cup, a small negative repelling voltage ($\sim 150\text{V}$) is applied to the suppressor ring.

The stainless steel Faraday cups used for LEBIT are shown in fig. 5.10. The picture shows the cup in different stages of the assembly process.

Fig. 5.11 shows the Faraday cup mounted to its 6" conflat flange. The



Figure 5.10: Photograph of Faraday cup during assembly

pneumatic device that moves the cup in and out can be seen on the right.

For the signal readout a logarithmic amplification has been chosen. The so module converts incoming signals between 100fA and 1nA , caused by the positive ion current, into a corresponding voltage output of 1V to 10V . During the measurements it was verified that the Faraday cup in combination with the logarithmic amplifier was able to detect currents as low as some hundred fA .

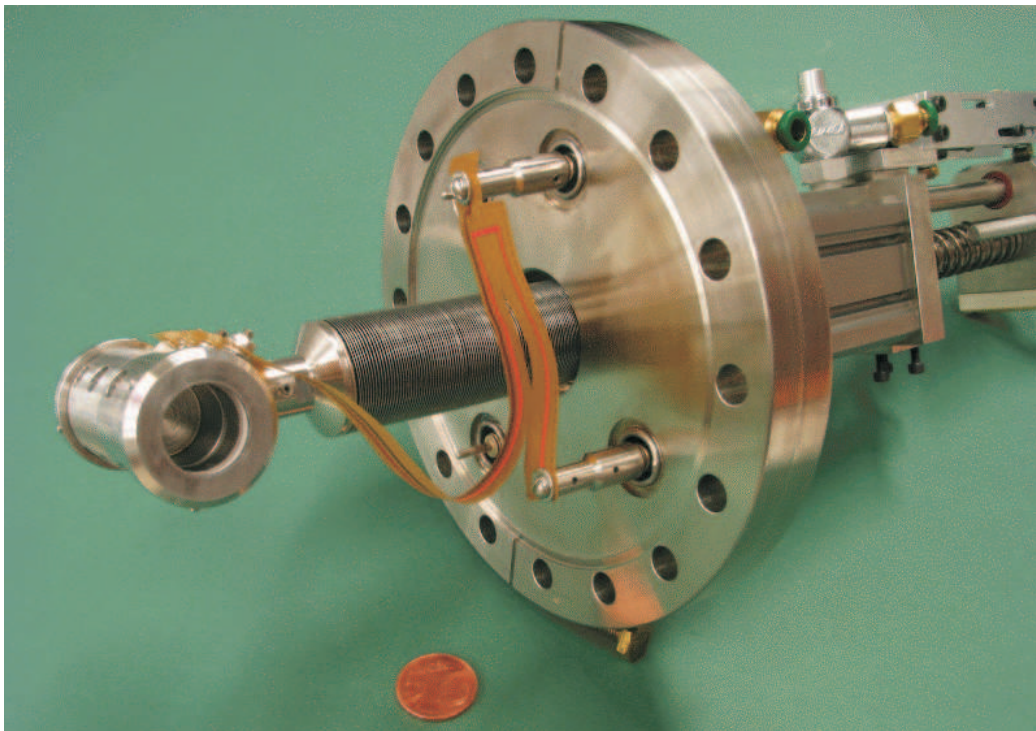


Figure 5.11: Assembled Faraday cup. Flexible capton boards connect voltage and signal connectors with vacuum feedthroughs.

Chapter 6

Summary and Conclusion

LEBIT is a novel project with the potential to combine high precision experiments at low energies with the benefits of high energy exotic isotope production at the NSCL. For the calibration of the Penning Trap, cooler and buncher, and testing of the beam transport and beam imaging system, a stable and, sometimes mass separated pilot beam is needed.

Setting up an ion source for the production of a stable beam and development of a Wien filter for mass separation was part of this work, as well as implementing a beam observation system based on micro channel plates and Faraday cups. The properties of the constructed Wien filter were measured and the pilot beam was used to test the electrostatic beam transport and beam imaging system.

The Wien filter is a small and compact device capable of a modest resolving power. Its main feature is the use of permanent magnets to create the magnetic field. A special design for the electrode structure creating the electric field is necessary to maintain a constant E/B ratio.

The microchannel plate detector system uses two plates which have a combined gain of 10^7 and image the beam to a phosphore screen, where the image is read by a digital camera. It could be shown, that the imaging system works, even for low ion currents.

The Faraday cups are capable of detecting currents as low as 100pA. Using the beam observation system it was verified that the beam transport system works as planned.

Determination of the Wien filters resolving power for different beam en-

ergies showed that it is lower than theoretically expected, but still within reasonable range.

The reason for the deviation can most likely be determined if more detailed studies of the ions source properties are performed. The ion source is a commercially available model. It changed its behavior frequently over time and was a source of constant surprises.

More detailed understanding of the source properties will most likely allow the enhancement of the resolving power of the filter. Further improvement can be achieved by increasing the magnetic field. This would lead to a higher resolving power, especially for heavier masses. Additional enhancements can be made with changes to the electrode structure. The important E/B ratio is not perfectly constant with the current setup. A higher resolution stripe electrode structure could improve the ratio. Alternatively, it can be examined if a plate capacitor with a small distance between the plates can replace the whole electrode structure and achieve better results.

In conclusion, it can be stated that beam transport and observation function as expected. The ion source is operating, but requires further studies. The Wien filter is working and has room for future improvements.

Chapter 7

Appendix

7.1 Appendix A: Electronic wirerings

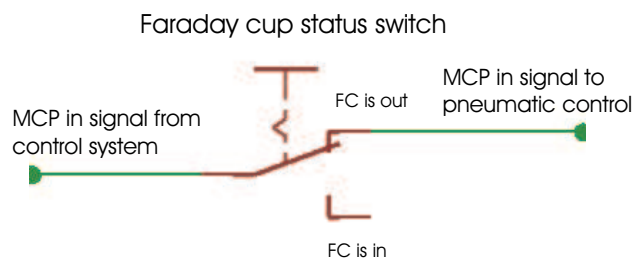


Figure 7.1: Safety wiring for MCP detector. The signal "move the MCP in" is only allowed to continue to the pneumatic control if the Faraday cup detector is in its "moved out" position.

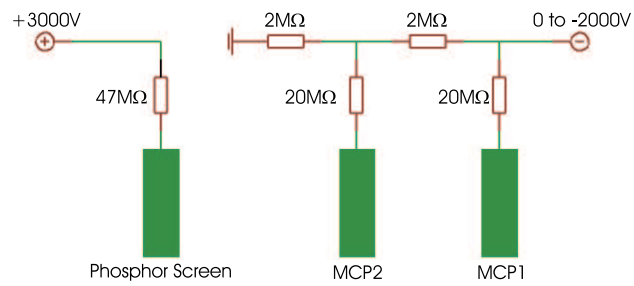


Figure 7.2: Electric connections for the MCPs and phosphor screens. The $2\text{M}\Omega$ resistors function as a voltage divider. The $20\text{M}\Omega$ and $47\text{M}\Omega$ resistors protect the plates and phosphor screen from damage through sparks.

7.2 Appendix B: Data sheets

Table 7.1: Camera properties summary

Imaging Device	1/3" Sony CCD
Color Depth	Black and White
Resolution	640x480
Scan method	progressive scan
Supported Frame Rates	3.75, 7.5, 15, 30
Minimum Illumination	<1.0lux
Brightness	-3dB to 33dB
Exposure	1/25s to 1/15000s
Trigger	yes

Table 7.2: MCP properties summary

Outside diameter	24.77mm
Imaging area	19mm diameter
Channel diameter	10 μ m
Center to center	12 μ m
Spatial resolution (single MCP)	42lp/mm
α	40
Bias angle	5 $^\circ$
Thickness	0.43mm
Flatness	≤ 0.08 mm
Gain	
Front MCP (1000V)	6.7 10^3
Rear MCP (1000V)	5.3 10^3
Total (1000V)	3.6 10^7
Dark Current	$\leq 5 \cdot 10^{-12}$ A
Beam Energy Range	1eV to over 50keV
Beam Current Range	<10 μ A (with grids)
Vacuum requirement	10 $^{-6}$ Torr or better
Max. bakeout temp.	350C

Acknowledgment

I would like to use these lines to thank all those who made this work possible and helped to make it a success.

First of all I would like to thank Prof. Hans-Joachim Körner and Prof. Konrad Gelbke, who made my stay at Michigan State University possible.

Furthermore I would like to thank Prof. Georg Bollen and Prof. Reiner Krücken, who made it possible, that I could use my work towards my Diploma degree. Georg Bollen earns my special thanks for giving me my thesis subject and my special appreciation for his steady support, advice and patience, as well as his help and dedication when it came to the write-up of this thesis.

I also would like to thank Dr. Stefan Schwarz, for teaching me many new skills and for all the time we spent on various discussions.

I would like to thank the whole LEBIT crew, for being good friends and co-workers. I really enjoyed the time with you.

I would like to thank, Jim Moskalik and Don Lawton for their help with the design of the Wien filter and the detector system.

Frederick Sharp earns my thanks for double checking grammar and spelling of this work.

Finally I'd like to thank all those who helped finishing this thesis but have not been mentioned by name: All the mechanics, electricians, welders and people working for the computer department.

Bibliography

- [1] T. Baumann; "The NSCL Coupled Cyclotron Project: Status and Latest News"; Proceedings of the Sixteenth International Conference on the Application of Accelerators in Research and Industry, Denton, Te, edited by J.L. Duggan, and I.L. Morgan; (American Institute of Physics, Melville, New York, 2001), p. 635
- [2] H. Koivisto, J. DeKamp, and A. Zeller; "Cooling of the Plasma Chamber for the AECR-U Type Electron Cyclotron Resonance Ion Source ARTEMIS"; Nucl. Instrum. Meth. B 174 (2001) 373.
- [3] A.F. Zeller, J.C. DeKamp, J. Wagner, and D. Capelli; "Construction and Testing of Superferric Dipoles for the A1900 Fragment Separator"; IEEE Transactions on Applied Superconductivity 11 (2001) 1725.
- [4] S. Schwarz et al.; "The low-energy-beam and ion-trap facility at NSCL/MSU"; TRIUMF (EMIS-14) 14th International Conference on Electromagnetic Isotope Separators and Techniques Related to Their Applications (EMIS-14) ; Victoria, B.C. Canada ; May 6-10, 2002
- [5] J. Schönfelder et al.; "SHIPTRAP a capture and storage facility for heavy radionuclides at GSI"; Nucl. Phys. A, 701, 579c, (2002)
- [6] Clark, J. et al.; "Improvements in the injection system of the Canadian penning trap mass spectrometer"; TRIUMF (EMIS-14) 14th International Conference on Electromagnetic Isotope Separators and Techniques Related to Their Applications (EMIS-14) ; Victoria, B.C. Canada ; May 6-10, 2002

- [7] P. Campbell, A. Nieminen, J. Billowes, P. Dendooven, K. T. Flanagan, D. H. Forest, Yu.P. Gangrsky, J.A.R. Griffith, J. Huikari, A. Jokinen, I.D. Moore, R. Moore, H.L. Thayer, G. Tungate, S.G. Zemlyanoi, J. Äystö; "First results from laser spectroscopy on bunched radioactive beams from the JYFL ion-beam cooler"; *European Physics Journal A* 15 (2002) 45-48.

- [8] T. von Egidy, P. Kienle, U. Köster, D. Habs, M. Groß, O. Kester, H.-J. Maier, P. G. Thirolf, and the MAFF collaboration; "The Munich Accelerator for Fission Fragments (MAFF) at the New Reactor FRM-II"; *acta physica slovacica* vol. 49 No. 1 (1999) 107-116

- [9] S. Schwarz et al.; "A second generation buncher and cooler"; TRIUMF (EMIS-14) 14th International Conference on Electromagnetic Isotope Separators and Techniques Related to Their Applications (EMIS-14) ; Victoria, B.C. Canada ; May 6-10, 2002

- [10] G. Bollen, S. Schwarz; "Ion traps for radioactive beam manipulation and precision experiments"; TRIUMF (EMIS-14) 14th International Conference on Electromagnetic Isotope Separators and Techniques Related to Their Applications (EMIS-14) ; Victoria, B.C. Canada ; May 6-10, 2002

- [11] T. Sun, Preliminary thesis, NSCL/MSU

- [12] M. Menzinger, L. Wahlin; "High intensity, low energy spread ion source for chemical accelerators"; *Review of scientific instruments* 40 (1968) 102.

- [13] W. Wien, *Ann. Phys. Chem.*, 65 (1898) 440.

- [14] S. Numela; Doctor's thesis; University of Jyväskylä

- [15] E. Gelfort; "Das Separationsvermögen des Wien-Filters"; *International Journal of Mass Spectrometry and Ion Physics*, 14 (1974) 349-361

- [16] Bu. Wrenger, K. H. Meiwes-Broer; "The application of a Wien filter to mass analysis of heavy clusters from a pulsed supersonic nozzle source";

Rev. Sci. Instrum. 68 (5), May 1997, 2027-2029

- [17] R. Holsinger, Lawrence Berkeley Laboratory, U.S.A., Swiss Institute for Nuclear Research (SIN), Switzerland, CERN, Switzerland, and Los Alamos National Laboratory, U.S.A; "Poisson Superfish Code"; <http://laacg1.lanl.gov/>
- [18] K. Bertsche, J.-F. Ostiguy and W.B. Foster; "Temperature considerations in the design of a permanent magnet storage ring"
- [19] www.stanfordmagnets.com
- [20] C. Kittel; "Introduction to Solid State Physics"; New York, Wiley, 1976.
- [21] J. L. Wiza; "Microchannel plate detectors"; Nuclear Instruments and Methods 162 (1979) 587.